

AI Alignment in Medical Imaging: Unveiling Hidden Biases Through Counterfactual Analysis

Haroui Ma^{†1}, Francesco Quinzan^{*†2}, Theresa Willem³, Stefan Bauer^{1,3}

¹School of Computation, Information and Technology, Technical University of Munich

²Department of Engineering Science, University of Oxford

³Helmholtz AI, Munich, Germany

[†]*equal contribution*

Abstract

Machine learning (ML) systems for medical imaging have demonstrated remarkable diagnostic capabilities, but their susceptibility to biases poses significant risks, since biases may negatively impact generalization performance. In this paper, we introduce a novel statistical framework to evaluate the dependency of medical imaging ML models on sensitive attributes, such as demographics. Our method leverages the concept of counterfactual invariance, measuring the extent to which a model’s predictions remain unchanged under hypothetical changes to sensitive attributes. We present a practical algorithm that combines conditional latent diffusion models with statistical hypothesis testing to identify and quantify such biases without requiring direct access to counterfactual data. Through experiments on synthetic datasets and large-scale real-world medical imaging datasets, including CHEXPERT and MIMIC-CXR, we demonstrate that our approach aligns closely with counterfactual fairness principles and outperforms standard baselines. This work provides a robust tool to ensure that ML diagnostic systems generalize well, e.g., across demographic groups, offering a critical step towards AI safety in healthcare. Code: <https://github.com/Neferpitou3871/AI-Alignment-Medical-Imaging>.

1 Introduction

A major problem in using machine learning (ML) systems for healthcare is that these systems exhibit biases leading to disparities in performance for different groups of patients [Adamson and Smith, 2018, Navarrete-Dechent et al., 2018, Sarkar et al., 2021, Seyyed-Kalantari et al., 0121]. For instance, patients from certain demographic groups may be more likely to be incorrectly classified as sick when healthy or health as sick. One possible reason for this problem is that AI models inadvertently learn and amplify existing confounding effects from the training data Banerjee et al. [2021].

With recent evidence that ML models can identify demographic factors such as age, sex, and racial identity from medical images—a skill beyond human capabilities—tracking confounding effects contained in medical imaging ML models is non-trivial Banerjee et al. [2021], Eng et al. [2021], Munk et al. [2021], Poplin et al. [2018], Rim et al. [2020], Yi et al. [2021]. Although the exact mechanisms of demographic group membership prediction remain unclear [Banerjee et al., 2021], the observable capability suggests that AI models can learn to correctly correlate certain features from medical image data to real-world demographic attributes, relying on proxies or imaging-related surrogate covariates that correlate with spECAfic attributes. These learned correlations, which may represent unfair treatment and discrimination in the real world, can distort a model’s performance and induce harmful biases. When applied in clinical

*Part of this work was done while Francesco Quinzan was employed at the Department of Computer Science, University of Oxford.

practice, models entailing such undetected biases may result in underdiagnosis and, thus, undertreatment.

In this paper, we present a statistical test to assess the dependency of imaging AI models on sensitive attributes, such as demographics. This method allows us to evaluate whether a diagnostic model has learned to interpret certain visual features as indicators for sensitive attributes, and use these interpretations for its predictions, *even if there is no causal relationship between these sensitive attributes and the development of a disease*. Our method is based on the notion of counterfactual invariance [Fawkes and Evans \[2023a\]](#), [Fawkes et al. \[2022b\]](#), [Quinzan et al. \[2022\]](#), [Veitch et al. \[2021\]](#). Intuitively, counterfactual invariance measures to which extent a model’s prediction remains unchanged when an attribute is altered. Counterfactual invariance explicitly removes the natural dependence between A and its causes, *ensuring that the relationship between A and the model’s predictions is not confounded by factors upstream of A* .

Our Contribution.

- We introduce a novel statistical test (Alg. 1) based on a robust theoretical framework to assess the dependency of medical imaging AI models on sensitive attributes, leveraging the concept of counterfactual invariance (Def. 4.1).
- To implement our statistical test, we design a latent diffusion model with disentangled representation that generates high-fidelity counterfactual images with perturbed sensitive feature while preserving disease-related features (Sec. 5).
- Experiments on synthetic datasets and real-world medical imaging datasets show that our method achieves strong alignment with counterfactual invariance principle, and that it outperforms baselines (Sec. 6).

2 Related Work

Counterfactual Invariance. Various notions of counterfactual invariance have been proposed in recent years. Almost sure counterfactual invariance means that a variable remains unchanged almost surely, with respect to changes to another variable [[Fawkes et al., 2022a](#)]. [[Fawkes and Evans, 2023b](#), [Veitch et al., 2021](#)] study functional counterfactual invariance. According to this definition, a function is considered counterfactually invariant if its output behaves in the same way as in almost sure counterfactual invariance. Distributional counterfactual invariance [[Fawkes and Evans, 2023b](#)], on the other hand, requires that the probability of distribution of outcomes remains the same under different interventions, rather than the outcomes themselves. Finally, [[Quinzan et al., 2024](#)] studies a generalization of distributional counterfactual invariance, by considering conditional distributions instead. The prECAse definitions of these notions are deferred to App. B.

Counterfactually Invariant Learner. A key approach of achieving counterfactually invariant learner is learning counterfactual invariant representations [[Pogodin et al., 2023](#), [Quinzan et al., 2024](#)]. [Pogodin et al. \[2023\]](#) introduces a neural representation that satisfies certain conditional independence conditions. However, their method uses the Hilbert-Schmidt norm of the kernel covariance as penalty during training. This approach may suffer from high variance, and it may be inapplicable to high-dimensional settings. As for the paper by [Quinzan et al. \[2024\]](#), its method targets counterfactual invariance during the training phase. In contrast, our approach is designed to quantify counterfactual invariance in a pretrained model.

Diffusion-Based Generative Models. Diffusion models (DMs) [Ho et al. \[2020a\]](#), [Rombach and Blattmann \[2022\]](#), [Sohl-Dickstein and Weiss \[2015\]](#) have shown immense versatility and effectiveness across various low-level vision tasks. [Sohl-Dickstein et al. \[2015\]](#) introduced

diffusion models with a convolutional architecture. Austin et al. [2021] extended this to discrete diffusion models, achieving competitive results. Ho et al. [2020b] improved the reverse diffusion process by estimating noise, while Nichol and Dhariwal [2021b] introduced better noise scheduling for faster sampling. Song et al. [2021] replaced the Markov process with a non-Markovian one, leading to faster sampling. In conditional generation, Dhariwal and Nichol [2021a] introduces classifier guidance, while Bordes et al. [2022] proposes diffusion models that are conditioned on self-supervised representations. Pandey et al. [2021], Sehwal et al. [2022] focus on generating images from low-density regions and using VAEs for controllable image generation, respectively. Ho et al. [2022] introduces Cascaded Diffusion Models for high-resolution image generation.

Fairness metrics in machine learning One of the earliest fairness metrics in machine learning is *fairness through unawareness*, which ignores protected attributes like race and gender. However, this is ineffective since such attributes are often encoded in other features [Hardt et al., 2016]. **Demographic Parity (DP)** refers to the statistical parity of outputs between demographic groups but has been criticized for practically not ensuring fairness Dwork et al. [2012], Hardt et al. [2016], making it unsuitable to medical classification cases. **Equality of Opportunity (EO)** aims for individual fairness but relies on similarities between cases, which are difficult to define in practice Dwork et al. [2012], Fleisher [2021]. **Counterfactual Fairness (CF)** offers an alternative by ensuring dECAsions are the same in both real and counterfactual worlds where demographics differ Kusner et al. [2017a].

AI Fairness in Medical Setting Several works have broadly discussed the application of AI fairness on medical datasets. Some prominent examples include: (1) [A. et al., 2022] offers a review on fairness in medical imaging but does **not** propose a novel evaluation method, focusing only on association-based metrics like DP/EO. (2) [Yang et al., 2024] investigates the role of demographic encodings and shares our fairness goal, but relies on EO, which we critique. (3) [Gadgil et al., 2024] uses explainability tools to analyze predictions of protected attributes but lacks a quantitative bias measure. (4) [Glocker et al., 2023] explores encoding and performance disparities but introduces no new methodology, unlike our statistical testing framework. To summarize, existing methods either rely on non-causal metrics or lack a quantified test framework.

3 Preliminaries

3.1 Background on Causality

The proposed statistical test and the related notion of Counterfactual Invariance use the language of probabilistic causality and structural causal models (SCMs, see Bongers et al. [2021], Pearl [2000]). This allows us to reason about the cause-effect relationships between features of a dataset, seen as random variables (r.vs.). Following Bongers et al. [2021], we define the causal structure of a dataset in terms of direct causal effects among the features. Direct causal effects are defined by distribution changes due to *interventions* on the DGP. An intervention amounts to actively manipulating the generative process of a feature in the dataset, without altering the remaining components of the DGP. In this work, we consider perfect interventions $A \leftarrow a$, by which the values of a feature A are set to a constant $A \equiv a$. We use the standard notation $do(A = a)$ to denote such an intervention. We refer the reader to App. A for the preCAs concepts introduced in this section.

3.2 Conditional Latent Diffusion Models (CLDMs)

Similar to latent diffusion models [Müller-Franzes et al., 2023a, Packhäuser et al., 2023, Pinaya et al., 2022, Rombach et al., 2022], CLDMs are a class of generative models that perform

diffusion processes in a lower-dimensional latent space, conditioned on additional information, enabling efficient and scalable generation of high-quality images tailored to spECAfic conditions or inputs [Jiang et al., 2023]. We use the notation $(E_\eta, D_\eta, p_\theta, q_\theta)$ to denote a CLDM, where E_η, D_η are an encoder-decoder modules, and q_θ, p_θ are the forward and reverse distributions of the latent diffusion model.

CLDMs utilize an encoder E_η to map input image X into a latent space, conditioned on A , where a diffusion process is conducted on the conditional latent representation $\mathbf{z}_0 = E_\eta(A, \mathbf{Z})$. The diffusion process in the conditional latent space consists of a forward process (diffusion) and a reverse process (denoising), similar to non-conditional models. Given a data distribution $q(\mathbf{z}_0 | \mathbf{c})$ on the latent space, the forward process sequentially adds noise to the data over a series of steps, producing a sequence of increasingly noisy samples $\mathbf{z}_1, \mathbf{z}_2, \dots, \mathbf{z}_T$, conditioned on a , where T represents the total number of steps. This process progressively transforms the original data into pure noise, setting the foundation for the subsequent reverse denoising process. In the forward process, Gaussian noise is iteratively added according to a Markov chain defined as:

$$q(\mathbf{z}_t | \mathbf{z}_{t-1}, a) = \mathcal{N}(\mathbf{z}_t; \sqrt{1 - \beta_t} \mathbf{z}_{t-1}, \beta_t \mathbf{I}),$$

where β_t is a variance schedule controlling the amount of noise added at each step t . As t increases, \mathbf{z}_t becomes a pure noise distribution as $t \rightarrow T$. The reverse process, conversely, denoises the noisy sample \mathbf{z}_t back to the original sample \mathbf{z}_0 , conditioned on a . The reverse process is defined as a series of conditional probabilities:

$$p_\theta(\mathbf{z}_{t-1} | \mathbf{z}_t, a) = \mathcal{N}(\mathbf{z}_{t-1}; \mu_\theta(\mathbf{z}_t, t, a), \Sigma_\theta(\mathbf{z}_t, t, a)), \quad (1)$$

where μ_θ and Σ_θ are the mean and covariance of the Gaussian distribution, parameterized by a neural network with parameters θ and conditioned on \mathbf{c} . Once the diffusion process is conducted on the latent space, CLDM generates a reconstructed image \hat{X} using a decoder D_η , by applying the decoder $\hat{X} = D_\eta(\mathbf{z}_0, a)$ to the latent sample \mathbf{z}_0 obtained by denoising \mathbf{z}_T .

Training. The training of a CLDM also involves two phases. In the first phase, the encoder E_η and a decoder D_η are trained to learn a meaningful latent space representation that incorporates the conditioning variable a . In this work, we use a standard VAE with an isotropic Gaussian prior $\mathcal{N}(0, \mathbf{I})$ on the latent space. In order to train E_η and D_η we use the standard ELBO as in Kingma and Welling [2014].

In the second phase, the diffusion model is trained within the conditional latent space. This involves training the neural network that parameterizes μ_θ and Σ_θ as in (1). Following standard training objectives, the model learns the optimal parameters θ by maximizing the following ELBO on the log-likelihood of the data:

$$\log p_\theta(\mathbf{z}_0 | a) \geq \mathbb{E}_q \left[\log \frac{p_\theta(\mathbf{z}_{0:T} | a)}{q(\mathbf{z}_{1:T} | \mathbf{z}_0, a)} \right] \quad (2)$$

This objective encourages the model to learn the reverse process that reconstructs the original data from noise, conditioned on a , by minimizing the KL-divergence between the true posterior and the model’s approximation.

Generation. During generation, the model starts with a sample from the noise distribution $\mathbf{z}_T \sim \mathcal{N}(0, \mathbf{I})$ and iteratively applies the learned reverse diffusion steps, conditioned on a , to generate a sample \mathbf{z}_0 . Each step denoises the current noisy sample based on the learned parameters μ_θ and Σ_θ , progressively refining the vector until a clear, noise-free data point is obtained. The decoder D_η is then applied to \mathbf{z}_0 , along with a , to generate a new data point.

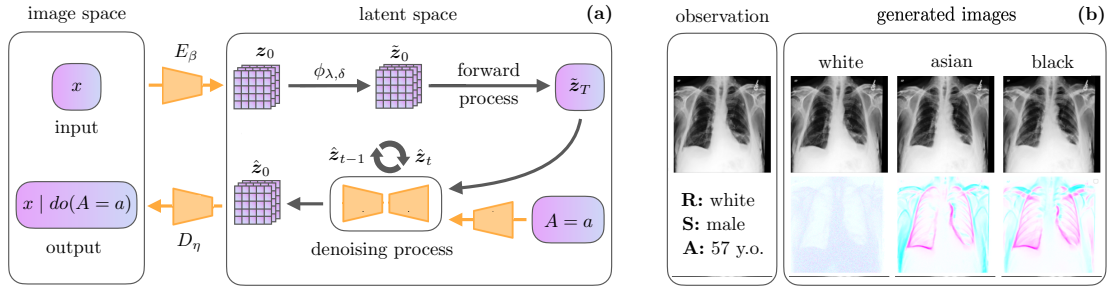


Figure 1: **(a)** Visualization of the conditional latent diffusion model used in Alg. 1. **(b)** Examples of generated images using the CLDM of Alg. 1 under different conditioning labels. The bottom row highlights differences between the original image and the generated images. Larger counterfactual images are presented in App. J.

3.3 CLDMs with Disentangled Representations

In order to improve generation performance, we combine the standard CLDM framework (Sec. 3.2) with a non-linear transformation $\phi_{\lambda, \delta}$ on the representation space, to disentangle the CLDM representation vector from the chosen conditioning attribute $A = a$. This additional step ensures that the conditional model generates images that are consistent with the conditional label $A = a$. More concretely, the transformation $\phi_{\lambda, \delta}$ ensures that the representation \mathbf{Z} is approximately independent of the label A , i.e., $\mathbf{Z} \perp\!\!\!\perp A$. A visualization of the disentangled CLDM is presented in Fig. 1. We train the desired nonlinear transformation $\phi: \mathbf{z}_0 \rightarrow \tilde{\mathbf{z}}_0$, by considering a parametric family of transformations $\phi_{\lambda, \delta}(\mathbf{z}_0) = \mathbf{z}_0 + \lambda m_\delta(\mathbf{z}_0) / \|m_\delta(\mathbf{z}_0)\|$. Here, λ as a scalar to control the perturbation and m_δ is a neural network parameterized by δ . Here, $\|\cdot\|$ is the standard ℓ_2 norm. We choose parameters λ, δ such that the Mutual Information $I(\phi_{\lambda, \delta}(\mathbf{z}_0), a)$ is the lowest. Since the Mutual Information is generally intractable, we instead use a lower-bound, following Belghazi et al. [2018]. This lower-bound leverages dual representations of the KL-divergence, as

$$I(\phi_{\lambda, \delta}(\mathbf{z}_0), a) \geq \max_{\theta} \mathbb{E}[T_\theta(\phi_{\lambda, \delta}(\mathbf{z}_0), a)] - \log \left(\mathbb{E}_{\mathbf{Z}} \left[\mathbb{E}_A [e^{T_\theta(\phi_{\lambda, \delta}(\mathbf{z}_0), a)}] \right] \right), \quad (3)$$

where T_θ is a Neural Network (see App. C for details). Hence, the optimization objective becomes

$$\min_{\lambda, \delta} \max_{\theta} \mathbb{E}[T_\theta(\phi_{\lambda, \delta}(\mathbf{z}_0), a)] - \log \left(\mathbb{E}_{\mathbf{Z}} \left[\mathbb{E}_A [e^{T_\theta(\phi_{\lambda, \delta}(\mathbf{z}_0), a)}] \right] \right)$$

This is a min-max optimization problem. We propose to use an alternative optimization schedule to optimize (4). In App. I we show that in our experimental framework, using disentangled representations improves generation performance.

4 Methodology

4.1 Notation

We denote with f a base classifier or categorical model of interest, and we denote with X a random variable that corresponds to its input. The outcome of f is denoted with $\hat{Y} = f(X)$ which corresponds to categorical labels for the inputs. We also denote with A, Z_1, Z_2, \dots, Z_n a set of features for the images X . These features, which may be both observed and unobserved, represent various aspects of the image, such as pixel values, color channels, edges, textures, or more abstract representations. The attribute A is a sensitive attribute that should not influence the outcome \hat{Y} of the given base model f . Throughout this work, we also use the notation $\mathbf{Z} := \{Z_1, Z_2, \dots, Z_n\}$, to denote all the features of X that are not considered a sensitive attribute. As mentioned in Sec. 3.1, we use the notation $do(A = a)$ to denote an intervention on the feature A .

4.2 Counterfactual Invariance (CI)

We propose to test the robustness of a ML model using the notion of CI. In our setting, CI is a state in which an ML model’s predictions remain unchanged when, in a hypothetical scenario, a spECAFic input variable is altered. As a property of an ML model, CI applies to spECAFic input variables. For instance, if an ML model is counterfactually invariant to the racial input variable, the prediction for a given input should remain the same regardless of whether the racial variable changes from, say, "Black" to "White". Formally, a CI model is defined as follows.

Definition 4.1 (Counterfactual Invariance, following [Kusner et al. \[2017b\]](#), [Quinzan et al. \[2024\]](#)). A model $f(X)$ is said to be counterfactually invariant with respect to an attribute A if, for any input X with features $\mathbf{Z} = \mathbf{z}$, the predicted outcome $\hat{Y} := f(X)$ satisfies:

$$\mathbb{E}[\hat{Y} \mid do(A = a), \mathbf{Z} = \mathbf{z}] = \mathbb{E}[\hat{Y} \mid do(A = a'), \mathbf{Z} = \mathbf{z}] \quad (4)$$

for any possible value a' of the attribute A .

Intuitively, Def. 4.1 means that the expected prediction of the model given the intervention $do(A = a)$ is the same as that given $do(A = a')$, assuming that all other features are held constant. By revealing whether model predictions are affected by interventions on an attribute A that should not have causal relationships to the prediction \hat{Y} , CI helps detect biases, ultimately decreasing the risk of misdiagnosis for individuals and the exacerbation of existing disparities. As shown in the next paragraph, a major advantage of the CI notion in Def. 4.1 is that under additional assumptions it can be tested from samples. However, other definitions of CI have been studied in the literature, e.g., [Fawkes et al. \[2022a\]](#), [Veitch et al. \[2021\]](#). We discuss these definitions in Appendix B. In this work, we address the scenario where the feature labels $\mathbf{Z} = \mathbf{z}$ are potentially unknown, requiring us to learn their corresponding representation vectors. To achieve this, we employ conditional latent diffusion models, as discussed in Sec. 5.

Learning CI from samples. We provide a method to verify if a classifier is CI. We establish a connection between the notion of CI as in Def. 4.1 and quantities that can be directly estimated from samples, as detailed in the following lemma.

Theorem 4.2. *Define the functions $g(a, \mathbf{z}) := \mathbb{E}[\hat{Y} \mid A = a, \mathbf{Z} = \mathbf{z}]$ and $h(\mathbf{z}) := \mathbb{E}[\hat{Y} \mid \mathbf{Z} = \mathbf{z}]$, where \mathbf{Z} is the representation vector of a disentangled CLDM (Sec. 3.2-3.3). Then, a model $f(X)$ is counterfactually invariant with respect to an attribute A if and only if (iff.) it holds $\mathbb{E}[\hat{Y}g(A, \mathbf{Z})] = \mathbb{E}[\hat{Y}h(\mathbf{Z})]$. Here, the expected value on the left-hand side is taken over the joint random variables \hat{Y} , A , and \mathbf{Z} , whereas the expected value on the right-hand side is taken over \hat{Y} and \mathbf{Z} .*

This theorem tells us that, under the conditional ignorability of the protected attribute, a model $f(X)$ is counterfactually invariant with respect to an attribute A if and only if the expected value of $\hat{Y} \cdot g(A, \mathbf{Z})$ over \hat{Y}, \mathbf{Z}, A equals the expected value of $\hat{Y} \cdot h(\mathbf{Z})$ over \hat{Y}, \mathbf{Z} . A proof of this lemma is provided in Appendix D, and it follows [Quinzan et al. \[2023\]](#). Intuitively, Theorem 4.2 follows from the law of total variance, which quantifies how much \hat{Y} varies as A changes, after controlling for \mathbf{Z} . Crucially, the representation \mathbf{Z} is assumed to form a valid adjustment set.

5 Practical Algorithm

Testing CI. Theorem 4.2 suggests a way to test CI from samples. Instead of directly computing Eq. (4), we learn the functions $g(a, \mathbf{z})$ and $h(\mathbf{z})$ as in Theorem 4.2 from samples, and use a paired t -test to determine if $\mathbb{E}[\hat{Y}g(A, \mathbf{Z})] = \mathbb{E}[\hat{Y}h(\mathbf{Z})]$. SpECAFically, let $\mu_1 = \mathbb{E}[\hat{Y}\hat{g}(A, \mathbf{Z})]$

Algorithm 1 CI Test via Latent Representations (CIT-LR)

1: **Input:** training and test datasets $\mathbf{D}_{\text{TRAIN}}$, \mathbf{D}_{TEST} , and a base diagnostic model f ;
2: **Output:** p -value for the statistical test;
3: //
4: // (Step 1) Learn the functions $g(a, \mathbf{z})$ and $h(\mathbf{z})$ on $\mathbf{D}_{\text{TRAIN}} = \{x^{(j)}, a^{(j)}\}_j$
5: train a CLDM ($E_\eta, D_\eta, p_\theta, q_\theta$) together with a transformation $\phi_{\lambda, \delta}$ on $\mathbf{D}_{\text{TRAIN}}$ as in Sec. 3.3;
6: define $\hat{g}(a, \mathbf{z}) := \frac{1}{n} \sum_j f(x^{(j)})$ with $x^{(j)} \sim D_\eta(\hat{\mathbf{z}}_0^{(j)})$, $\hat{\mathbf{z}}_0^{(j)} \sim p_\theta(\hat{\mathbf{z}}_0 | \mathbf{z}, a)$;
7: define $\hat{h}(\mathbf{z}) := \frac{1}{n} \sum_j f(x^{(j)})$ with $x^{(j)} \sim D_\eta(\hat{\mathbf{z}}_0^{(j)})$, $\hat{\mathbf{z}}_0^{(j)} \sim p_\theta(\hat{\mathbf{z}}_0 | \mathbf{z})$;
8: //
9: // (Step 2) Estimate the mean and variance of the r.vs. $\hat{Y} \cdot g(A, \mathbf{Z})$ and $\hat{Y} \cdot h(\mathbf{Z})$ on $\mathbf{D}_{\text{TEST}} = \{x^{(i)}, a^{(i)}, \hat{y}^{(i)} = f(x^{(i)})\}_i$
10: $\hat{\mu}_{A, \mathbf{Z}} \leftarrow \frac{1}{|\mathbf{D}_{\text{TEST}}|} \sum_i \hat{y}^{(i)} \cdot \hat{g}(a^{(i)}, \hat{\mathbf{z}}_T^{(i)})$ with $\hat{\mathbf{z}}_T^{(i)} \sim q_\theta(\hat{\mathbf{z}}_T | \hat{\mathbf{z}}_0^{(i)})$, $\hat{\mathbf{z}}_0^{(i)} = \phi_{\lambda, \delta}(\mathbf{z}_0^{(i)})$, $\mathbf{z}_0^{(i)} \sim E_\eta(x^{(i)})$;
11: $\hat{\sigma}_{A, \mathbf{Z}} \leftarrow \frac{1}{|\mathbf{D}_{\text{TEST}}|} \sum_i (\hat{y}^{(i)} \cdot \hat{g}(a^{(i)}, \hat{\mathbf{z}}_T^{(i)}) - \hat{\mu}_{A, \mathbf{Z}})^2$ with $\hat{\mathbf{z}}_T^{(i)} \sim q_\theta(\hat{\mathbf{z}}_T | \hat{\mathbf{z}}_0^{(i)})$, $\hat{\mathbf{z}}_0^{(i)} = \phi_{\lambda, \delta}(\mathbf{z}_0^{(i)})$, $\mathbf{z}_0^{(i)} \sim E_\eta(x^{(i)})$;
12: $\hat{\mu}_{\mathbf{Z}} \leftarrow \frac{1}{|\mathbf{D}_{\text{TEST}}|} \sum_i \hat{y}^{(i)} \cdot \hat{h}(\hat{\mathbf{z}}_T^{(i)})$ with $\hat{\mathbf{z}}_T^{(i)} \sim q_\theta(\hat{\mathbf{z}}_T | \hat{\mathbf{z}}_0^{(i)})$, $\hat{\mathbf{z}}_0^{(i)} = \phi_{\lambda, \delta}(\mathbf{z}_0^{(i)})$, $\mathbf{z}_0^{(i)} \sim E_\eta(x^{(i)})$;
13: $\hat{\sigma}_{\mathbf{Z}}^2 \leftarrow \frac{1}{|\mathbf{D}_{\text{TEST}}|} \sum_i (\hat{y}^{(i)} \cdot \hat{h}(\hat{\mathbf{z}}_T^{(i)}) - \hat{\mu}_{\mathbf{Z}})^2$ with $\hat{\mathbf{z}}_T^{(i)} \sim q_\theta(\hat{\mathbf{z}}_T | \hat{\mathbf{z}}_0^{(i)})$, $\hat{\mathbf{z}}_0^{(i)} = \phi_{\lambda, \delta}(\mathbf{z}_0^{(i)})$, $\mathbf{z}_0^{(i)} \sim E_\eta(x^{(i)})$;
14: //
15: // (Step 3) Use a two-sample Student's t -test to determine if $\mathbb{E}[\hat{Y}g(A, \mathbf{Z})]$ is equal to $\mathbb{E}[\hat{Y}h(\mathbf{Z})]$.
16: Compute the p -value of the t -statistics $t = \sqrt{|\mathbf{D}_{\text{TEST}}|}(\hat{\mu}_{\mathbf{Z}} - \hat{\mu}_{A, \mathbf{Z}})/(\hat{\sigma}_{\mathbf{Z}} - \hat{\sigma}_{A, \mathbf{Z}})$ with $|\mathbf{D}_{\text{TEST}}| - 1$ degrees of freedom;
17: **return** the p -value of the statistical test;

and $\mu_2 = \mathbb{E}[\hat{Y}\hat{h}(\mathbf{Z})]$, where g and h represent the functions of interest, with A indicating a sensitive attribute. The hypothesis test is defined as:

$$\begin{aligned} \mathcal{H}_0 : \mu_1 &= \mu_2 && \text{(Ctf-Invariant w.r.t } A) \\ \mathcal{H}_1 : \mu_1 &\neq \mu_2 && \text{(Not Ctf-Invariant w.r.t } A) \end{aligned}$$

This approach is justified by Theorem 4.2, which states that $\mathbb{E}[\hat{Y}g(A, \mathbf{Z})]$ is equal to $\mathbb{E}[Yh(\mathbf{Z})]$ if and only if the underlying model $f(X)$ is counterfactually invariant with respect to an attribute A .

Overview of the algorithm. Our proposed approach to perform this test can be summarized in the following steps, based on Theorem 4.2 and the test discussed earlier:

1. Learn the functions $g(a, \mathbf{z})$ and $h(\mathbf{z})$ as in Theorem 4.2 using a disentangled CLDM.
2. Estimate the mean and variance of the random variables (r.vs.) $\hat{Y} \cdot g(A, \mathbf{Z})$ and $\hat{Y} \cdot h(\mathbf{Z})$.
3. Use a two-sample Student's t -test to determine if $\mathbb{E}[\hat{Y}g(A, \mathbf{Z})]$ is equal to $\mathbb{E}[Yh(\mathbf{Z})]$.

In practice, we perform step 1 and step 2 on different, approximately uncorrelated training datasets. This has the effect of limiting the bias induced by estimates of $g(a, \mathbf{z})$ and $h(\mathbf{z})$ (see, e.g., Chernozhukov et al. [2022], Newey and Robins [2018]).

We present a practical method to implement step 1-3. We call this method *CI Test via Latent Representations* (CIT-LR), and it is presented in Alg. 1. This algorithm aims to test whether a model is counterfactually invariant with respect to an attribute A , by implementing Step 1-3 of Sec. 5. Crucially, our algorithm uses a CLDM ($E_\eta, D_\eta, p_\theta, q_\theta$) together with a non-linear transformation $\phi_{\lambda, \delta}$ on the representations space, to generate images $\hat{\mathbf{x}}$ conditioned on attributes $a \sim A$ and $\mathbf{z} \sim Z$. The transformation $\phi_{\lambda, \delta}$ is introduced to disentangle the representations $\mathbf{z} \sim Z$ from the sensitive attribute, which improves generation performance (Sec. 3.3, App. I). A visualization of the CLDM, as well as the resulting DGP for image generation are shown in Fig. 1.

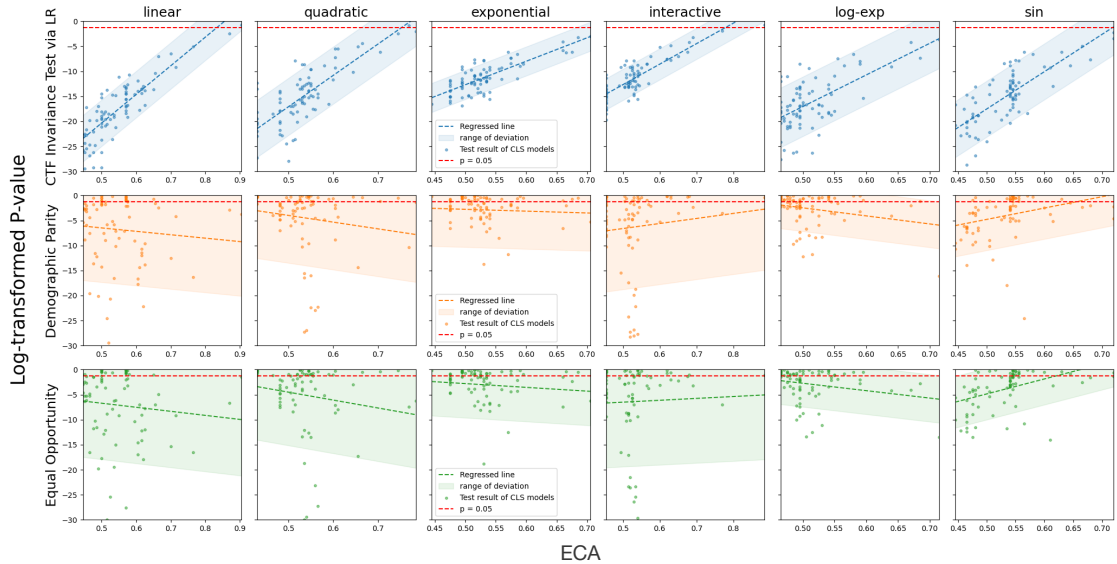


Figure 2: The relationship between log-transformed p -values and the ECA tested on synthetic datasets for 100 base classifiers (see App. G.1). Column names refer to the different synthetic datasets (see App. F.1). Each point represents the tested result of a spECAfic classifier. A straight line is fitted to highlight the Pearson correlation, and the parallel painted region shows the standard deviations of the p -values. The red dashed horizontal line represents a significance threshold at $\log(p) = \log(0.05)$. Our testing method aligns more consistently with the ground truth than baselines.

6 Experiments

The goal of these experiments is twofold. First, we show that our statistical test is aligned with the notion of CI as in Def. 4.1. Furthermore, we show that the CLDM as in Alg. 1 has good generation performance. To this end, we perform three rounds of experiments. We first consider synthetic dataset, for which the DGP are fully known. Then, we consider two real-world datasets, CHEXPART [Irvin et al., 2019] and MIMIC-CXR [Johnson et al., 2019a,b].

6.1 Overall Set-Up

Model architecture for the CLDM in Alg. 1. The encoder is constructed as a series of convolutional layers and downsampling modules, which progressively reduce the spatial dimensions while capturing essential features from the input data. The decoder, on the other hand, consists of convolutional layers and upsampling modules. To enhance the model’s performance, attention mechanisms and skip connections are employed. The DDPM uses U-net (see, e.g., [Ronneberger et al., 2015a, Siddique et al., 2021]) as the noise estimator $\epsilon_\theta(z_t, t, a)$ to denoise the latent space. Following Rombach and Blattmann [2022], the U-net is further augmented by a cross-attention mechanism to enable layer propagation with conditioned label. Further implementation details for the CLDM are shown in App. H.1

Baselines. We consider two popular fairness metrics for experimental comparison, namely **Demographic Parity (DP)** and **Equality of Opportunity (EO)**. DP is a fairness metric based on association. According to this metric, a model f is fair iff.

$$\mathbb{P}[f(X) = 1 \mid A = a] = \mathbb{P}[f(X) = 1 \mid A = a']. \quad (5)$$

To make it convenient for comparison, we transform DP into a statistical test, by conducting a paired t-test to determine if (5) holds. We consider a second metric, EO. This is another

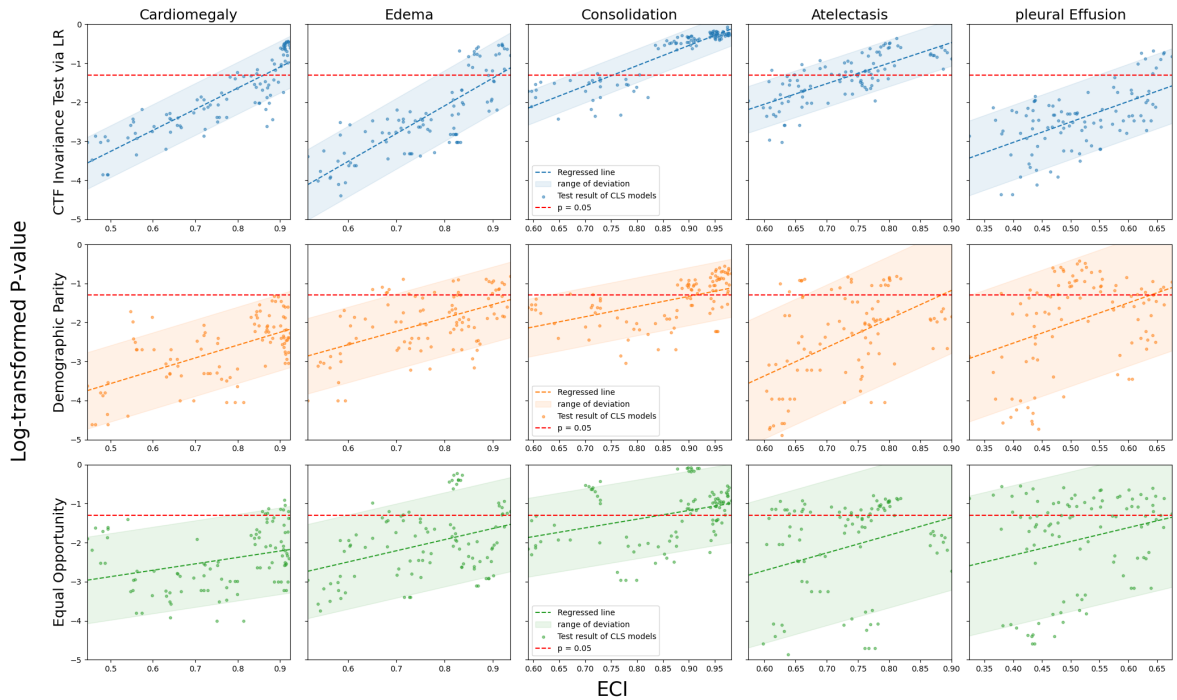


Figure 3: The relationship between log-transformed p -values and the ECA is examined using the CHEXPert dataset (Irvin et al. [2019], App. F.1) for 100 base classifiers (App. G.2). The column labels correspond to the various target diseases of the dataset. Each point represents the outcome of testing a spECAfic classifier. A straight line is fitted to illustrate the Pearson correlation, with a shaded area indicating the standard deviation of the p -values. A red dashed horizontal line marks the significance threshold at $\log(p) = \log(0.05)$. Our testing method aligns more consistently with the ground truth than baselines.

widely used metric, by which a model is fair iff. it holds

$$\mathbb{P}[f(X) = 1|Y = y, A = a] = \mathbb{P}[f(X) = 1|Y = y, A = a'] \quad (6)$$

Again we transform the criteria into a statistical test, by conducting a paired t-test to determine if (6) holds. Both DP and EO have been criticized, for either not ensuring fairness Dwork et al. [2012], Hardt et al. [2016], or relying on “similarity” attributes that are difficult to define in practice. We remark that DP and EO are purely based on statistical associations, and they do not rely on counterfactuals, as opposed to Def. 4.1.

Implementation. All the code is implemented using Python. For synthetic datasets, the algorithms are built on the statistical learning algorithms in the scikit-learn package. Since these experiments do not require much computational resources, they run on the CPU alone. For the two real-world medical image datasets, the experiments are run on a single 48GB Nvidia A100 GPU.

6.2 Synthetic Datasets

Dataset description. We consider six synthetic datasets which we call “linear”, “quadratic”, “exponential”, “interactive”, “log-scale”, and “sin”. Each dataset consists of features $\mathbf{Z} = \{Z_0, Z_1, \dots, Z_n\}$ and a protected attribute A , together with a r.v. X that depends on this features, and binary labels Y for X . We further generate labels Y for X . Here, features \mathbf{Z} are generated using an auto-regressive process. Each of the five synthetic datasets uses different structural equations, which are described in App. F.1.

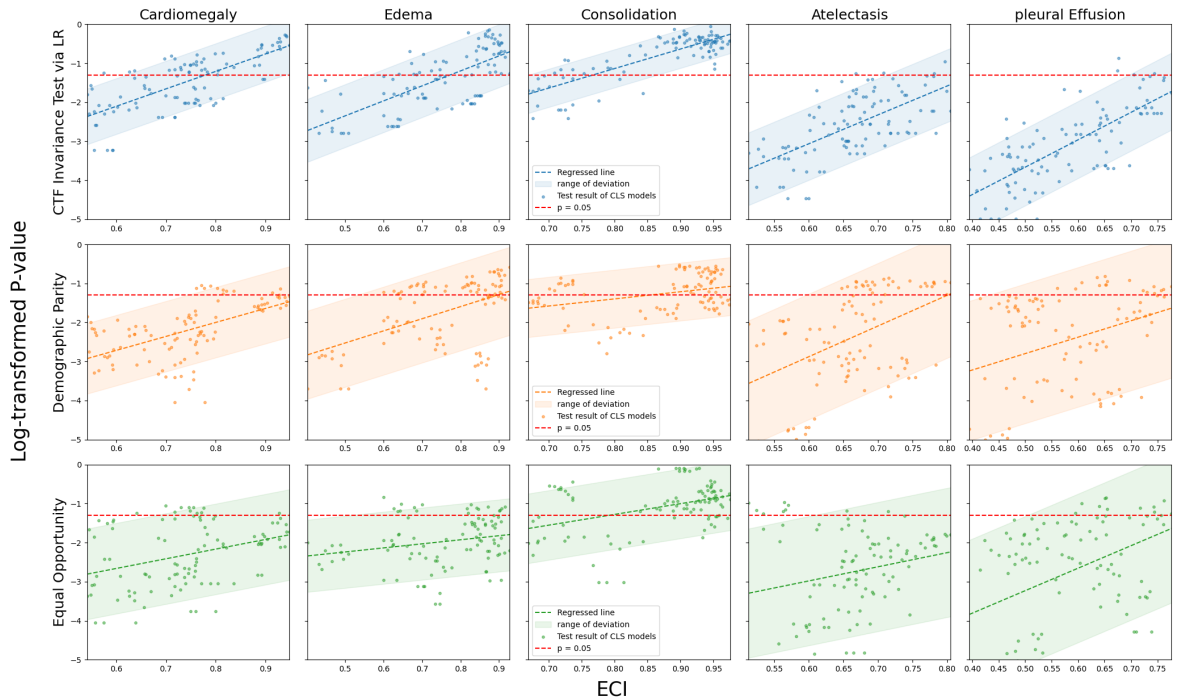


Figure 4: The relationship between log-transformed p -values and the ECA is examined using the MIMIC-CXR dataset (Johnson et al. [2019a,b], App. F.1) for 100 base classifiers (App. G.2). The column labels correspond to the various target diseases of the dataset. Each point represents the outcome of testing a spECAfic classifier. A straight line is fitted to illustrate the Pearson correlation, with a shaded area indicating the standard deviation of the p -values. A red dashed horizontal line marks the significance threshold at $\log(p) = \log(0.05)$. Our testing method aligns more consistently with the ground truth than baselines.

Performance Evaluation Metric. Our metric of interest is the *Expected Counterfactual Accuracy* (ECA). This metric quantifies CI as in Def. 4.1. To define ECA, consider indicator the function

$$\iota(a, \mathbf{z}) := \begin{cases} 1 & \text{if } \mathbb{E}[\hat{Y} | do(A = a), \mathbf{Z} = \mathbf{z}] = \mathbb{E}[\hat{Y} | \mathbf{Z} = \mathbf{z}] \\ 0 & \text{otherwise} \end{cases} \quad (6)$$

Then, the ECA is defined as

$$\text{ECA} := \mathbb{E}[\iota(a, Z)]. \quad (6)$$

Here, the expected value is taken over all possible representations $\mathbf{Z} = \mathbf{z}$, and $do(A = a)$, with a sampled uniformly at random from the set of all possible interventions on the attribute A . Note that if $\text{ECA} = 1$, then the intervention $do(A = a)$ does not have a causal effect beyond what is already accounted for by \mathbf{Z} , i.e., the model f is CI as in Def. 4.1.

Results on alignment with ECA. For each of the synthetic datasets, we consider 100 base classifiers as detailed in App. G.1. These base classifier take as input a datapoint $x \sim X$, and they predict its corresponding label \hat{y} . For each base classifier, we run Alg. 1 to determine if the given classifier is counterfactually invariant w.r.t. the attribute A . Additionally, we run DP and EO as discussed in Sec. 6.1. In Fig. 2 we display the results. Each plot in Fig. 2 displays the p -values for Alg. 1, DP and EO against the ECA, where the significance of all statistical tests is set to $\alpha = 0.05$. We clearly observe that the p -values of our statistical test are correlated with ECA, as opposed to DP and EO. Similarly, we observe that DP and EO are misaligned with CI as in Def. 4.1.

6.3 Real-World Datasets

Datasets description. We consider two large datasets consisting of radiological images, namely the CHEXPART dataset [Irvin et al., 2019], and the MIMIC-CXR [Johnson et al., 2019a,b] dataset. Both datasets consist of chest radiographs paired with radiological reports and demographic attributes of the patients, including the self-reported race.¹² Images in these datasets are labeled with various radiographic observations, including binary attributes for the presence of cardiomegaly, edema, consolidation, atelectasis, and pleural effusion. We refer to App. F.1 for a detailed descriptions of these datasets.

Performance Evaluation Metric. We use again the Expected Counterfactual Accuracy as detailed in Sec. 6.2. In this case, we can compute the ECA since it holds $\mathbb{E}[\hat{Y} \mid do(A = a), \mathbf{Z} = \mathbf{z}] = \mathbb{E}[\hat{Y} \mid A = a, \mathbf{Z} = \mathbf{z}]$. We refer the reader to App. E for a proof of this claim.

Results on alignment with ECA. For each dataset, we analyze 10 diagnostics as described in App. G.2. For each diagnostic model, we evaluate 10 different checkpoints with similar accuracies, resulting in a total of 100 classifiers. These classifiers receive a datapoint $x \sim X$ as input and predict the corresponding label \hat{y} . We apply Algorithm 1 to each base classifier to assess whether it is counterfactually invariant with respect to the attribute A . Furthermore, we evaluate DP and EO as outlined in Sec. 6.1. The results are presented in Fig. 3-4 (Fig. 4 is put in appendix), where each linearly fitted scatter plots the log-transformed p -values for Alg. 1, DP, and EO against the ECA. All statistical tests are performed with a significance level of $\alpha = 0.05$. In Fig.3, the p -values from the CIT-LR method exhibit higher correlation and lower variance than those of EO and DP. Notably, for strongly CTF-invariant diagnostic models on detecting Cardiomegaly and Consolidation, i.e., with relatively high ECA (≥ 0.8) in the first and third column, DP and EO reject almost all the models when they actually should **not**. Our CIT-LR, in contrast, successfully detect this invariance with yielding non-significant p -values. Furthermore, for strongly non-CTF-invariant models diagnosing pleural effusion, DP and EO often reject the hypothesis when they shouldn't. In contrast, the CIT-LR does not flag models with lower ECA as positive. **In sum, our CIT-LR rejects the hypothesis test when ECA is low and does not when the ECA is high, demonstrating a stronger consistency over EO and DP.** Similar considerations hold for the results displayed on Fig.4. Overall, the p -values from our statistical test correlate with ECA better than DP and EO.

7 Impact Statement

The proposed Counterfactual Invariance Test via Latent Representations has significant implications for fairness in medical AI. The method explores the deep causal mechanism of the diagnostic models, revealing dependencies, which are overlooked by traditional association-based metrics. Through quantifying the biases linked to the sensitive attribute, our method could check the diagnostic models' misbehavior across demographic groups, reducing the risk of misdiagnosis. Overall, this work advances responsible AI in healthcare, encouraging further improvement of AI fairness.

However, challenges are also present. For instance, the hard-to-control variance and complexity of diffusion models make the generative model hard to train. Importantly, our method relies on the key assumption that the latent representations capture all the relevant factors, which is not adequately proved. Furthermore, the assumption that certain attributes should be

¹Race and racial identity can be difficult attributes to define in practice [Krieger, 1987]. In this work, we define race as a social, political, and legal construct, shaped by the interaction between how others perceive an individual and their own self-identification. For our experiments, we rely on patients' self-reported race.

²In this work, we restrict the datasets to images with racial labels "asian", "black", and "white" for simplicity.

considered "protected" requires careful consideration. Consultation with medical professionals is advised to build an accurate causal understanding.

Future work should aim to refine these representations and address unobserved confounding and expand the methodology to cover a broader range of problems. We believe interdisciplinary collaboration is the key to driving reliable AI development in healthcare.

Acknowledgments

Francesco acknowledges funding from ELSA: European Lighthouse on Secure and Safe AI project (grant agreement No. 101070617 under UK guarantee). The authors gratefully acknowledge the Gauss Centre for Supercomputing e.V. (www.gauss-centre.eu) for funding this project by providing computing time through the John von Neumann Institute for Computing (NIC) on the GCS Supercomputer JUPITER | JUWELS [Jülich Supercomputing Centre \[2021\]](https://www.fz-juelich.de/ia/juwels) at Jülich Supercomputing Centre (JSC). This work has been supported by the German Federal Ministry of Education and Research (Grant: 01IS24082).

References

- A., R. L. M., Echeveste, R., and Ferrante, E. (2022). Addressing fairness in artificial intelligence for medical imaging. *Nature Communications*, 13(1):4581.
- Adamson, A. and Smith, A. (2018). Machine learning and health care disparities in dermatology. *JAMA Dermatology*, 154(11):1247–1248.
- Austin, J., Johnson, D. D., Ho, J., Tarlow, D., and van den Berg, R. (2021). Structured denoising diffusion models in discrete state-spaces. In *Proceedings of the NeurIPS*, volume 34, pages 17981–17993.
- Banerjee, I., Bhimireddy, A. R., Burns, J. L., Celi, L. A., Chen, L.-C., Correa, R., Dullerud, N., Ghassemi, M., Huang, S.-C., Kuo, P.-C., Lungren, M. P., Palmer, L. J., Price, B., Purkayastha, S., Pyrros, A., Oakden-Rayner, L., Okechukwu, C., Seyyed-Kalantari, L., Trivedi, H., Wang, R., Zaiman, Z., Zhang, H., and Gichoya, J. W. (2021). Ai recognition of patient race in medical imaging: a modelling study. *The Lancet. Digital health*, 4:e406 – e414.
- Belghazi, M. I., Baratin, A., Rajeswar, S., Ozair, S., Bengio, Y., Hjelm, R. D., and Courville, A. C. (2018). Mutual information neural estimation. In *Proceedings of the 35th International Conference on Machine Learning, ICML 2018, Stockholmsmässan, Stockholm, Sweden, July 10-15, 2018*, volume 80 of *Proceedings of Machine Learning Research*, pages 530–539. PMLR.
- Bongers, S., Forré, P., Peters, J., and Mooij, J. M. (2021). Foundations of structural causal models with cycles and latent variables. *The Annals of Statistics*, 49(5):2885 – 2915.
- Bordes, F., Balestrieri, R., and Vincent, P. (2022). High fidelity visualization of what your self-supervised representation knows about. *Transactions on Machine Learning Research*.
- Chernozhukov, V., Newey, W., Quintas-Martinez, V., and Syrgkanis, V. (2022). Riesznet and forestriesz: Automatic debiased machine learning with neural nets and random forests. In *International Conference on Machine Learning, ICML 2022, 17-23 July 2022, Baltimore, Maryland, USA*, volume 162 of *Proceedings of Machine Learning Research*, pages 3901–3914. PMLR.
- Dhariwal, P. and Nichol, A. (2021a). Diffusion models beat gans on image synthesis. In *Proceedings of NeurIPS*, volume 34, pages 8780–8794.

- Dhariwal, P. and Nichol, A. (2021b). Diffusion models beat gans on image synthesis. *NeurIPS*, pages 8780–8794.
- Donsker, M. and Varadhan, S. (1983). Asymptotic evaluation of certain markov process expectations for large time, iv. *Communications on Pure and Applied Mathematics*, 36(2):183–212.
- Dwork, C., Hardt, M., Pitassi, T., Reingold, O., and Zemel, R. (2012). Fairness through awareness. In *Proceedings of the 3rd innovations in theoretical computer science conference*, pages 214–226.
- Eng, D. K., Khandwala, N. B., Long, J., Fefferman, N. R., Lala, S. V., Strubel, N. A., Milla, S. S., Filice, R. W., Sharp, S. E., Towbin, A. J., Francavilla, M. L., Kaplan, S. L., Ecklund, K., Prabhu, S. P., Dillon, B. J., Everist, B. M., Anton, C. G., Bittman, M. E., Dennis, R., Larson, D. B., Seekins, J. M., Silva, C. T., Zandieh, A. R., Langlotz, C. P., Lungren, M. P., and Halabi, S. S. (2021). Artificial intelligence algorithm improves radiologist performance in skeletal age assessment: a prospective multicenter randomized controlled trial. *Radiology*, 301(3):692–699.
- Fawkes, J., Evans, R., and Sejdinovic, D. (2022a). Selection, ignorability and challenges with causal fairness. In *Conference on Causal Learning and Reasoning*, pages 275–289. PMLR.
- Fawkes, J. and Evans, R. J. (2023a). Results on counterfactual invariance. *CoRR*, abs/2307.08519.
- Fawkes, J. and Evans, R. J. (2023b). Results on counterfactual invariance. *arXiv preprint arXiv:2307.08519*.
- Fawkes, J., Evans, R. J., and Sejdinovic, D. (2022b). Selection, ignorability and challenges with causal fairness. In *1st Conference on Causal Learning and Reasoning, CLear 2022, Sequoia Conference Center, Eureka, CA, USA, 11-13 April, 2022*, volume 177 of *Proceedings of Machine Learning Research*, pages 275–289. PMLR.
- Fleisher, W. (2021). What’s fair about individual fairness? In *Proceedings of the 2021 AAAI/ACM Conference on AI, Ethics, and Society*, pages 480–490.
- Gadgil, S., DeGrave, A. J., Daneshjou, R., and Lee, S.-I. (2024). Discovering mechanisms underlying medical ai prediction of protected attributes. *medRxiv*.
- Glocker, B., Jones, C., Bernhardt, M., and Winzeck, S. (2023). Algorithmic encoding of protected characteristics in chest x-ray disease detection models. *EBioMedicine*, 89:104467.
- Hardt, M., Price, E., and Srebro, N. (2016). Equality of opportunity in supervised learning. *Advances in neural information processing systems*, 29.
- He, K., Zhang, X., Ren, S., and Sun, J. (2015). Deep residual learning for image recognition.
- Higgins, I., Matthey, L., Pal, A., Burgess, C. P., Glorot, X., Botvinick, M. M., Mohamed, S., and Lerchner, A. (2017). beta-vae: Learning basic visual concepts with a constrained variational framework. In *5th International Conference on Learning Representations, ICLR 2017, Toulon, France, April 24-26, 2017, Conference Track Proceedings*. OpenReview.net.
- Ho, J., Jain, A., and Abbeel, P. (2020a). Denoising diffusion probabilistic models. *NeurIPS*, pages 6840–6851.
- Ho, J., Jain, A., and Abbeel, P. (2020b). Denoising diffusion probabilistic models. In *Proceedings of NeurIPS*, volume 33, pages 6840–6851.
- Ho, J., Saharia, C., Chan, W., Fleet, D. J., Norouzi, M., and Salimans, T. (2022). Cascaded diffusion models for high fidelity image generation. *Journal of Machine Learning Research*, 23(47):1–33.

- Huang, G., Liu, Z., and Weinberger, K. Q. (2016). Densely connected convolutional networks. *CoRR*, abs/1608.06993.
- Irvin, J., Rajpurkar, P., Ko, M., Yu, Y., Ciurea-Ilcus, S., Chute, C., Marklund, H., Haghighi, B., Ball, R. L., Shpanskaya, K. S., Seekins, J., Mong, D. A., Halabi, S. S., Sandberg, J. K., Jones, R., Larson, D. B., Langlotz, C. P., Patel, B. N., Lungren, M. P., and Ng, A. Y. (2019). Chexpert: A large chest radiograph dataset with uncertainty labels and expert comparison. In *The Thirty-Third AAAI Conference on Artificial Intelligence, AAAI 2019, The Thirty-First Innovative Applications of Artificial Intelligence Conference, IAAI 2019, The Ninth AAAI Symposium on Educational Advances in Artificial Intelligence, EAAI 2019, Honolulu, Hawaii, USA, January 27 - February 1, 2019*, pages 590–597. AAAI Press.
- Jiang, L., Mao, Y., Wang, X., Chen, X., and Li, C. (2023). Cola-diff: Conditional latent diffusion model for multi-modal MRI synthesis. In *Medical Image Computing and Computer Assisted Intervention - MICCAI 2023 - 26th International Conference, Vancouver, BC, Canada, October 8-12, 2023, Proceedings, Part X*, volume 14229 of *Lecture Notes in Computer Science*, pages 398–408. Springer.
- Johnson, A. E. W., Pollard, T. J., Berkowitz, S. J., Greenbaum, N. R., Lungren, M. P., ying Deng, C., Mark, R. G., and Horng, S. (2019a). MIMIC-CXR, a de-identified publicly available database of chest radiographs with free-text reports. *Scientific Data*, 6.
- Johnson, A. E. W., Pollard, T. J., Greenbaum, N. R., Lungren, M. P., ying Deng, C., Peng, Y., Lu, Z., Mark, R. G., Berkowitz, S. J., and Horng, S. (2019b). MIMIC-CXR-JPG, a large publicly available database of labeled chest radiographs.
- Jülich Supercomputing Centre (2021). JUWELS Cluster and Booster: Exascale Pathfinder with Modular Supercomputing Architecture at Jülich Supercomputing Centre. *Journal of large-scale research facilities*, 7(A138).
- Kingma, D. P. and Welling, M. (2014). Auto-encoding variational bayes. In Bengio, Y. and LeCun, Y., editors, *2nd International Conference on Learning Representations, ICLR 2014, Banff, AB, Canada, April 14-16, 2014, Conference Track Proceedings*.
- Krieger, N. (1987). Shades of difference: theoretical underpinnings of the medical controversy on black/white differences in the united states, 1830-1870. *International Journal of Health Services*, 17(2):259–278.
- Kusner, M. J., Loftus, J., Russell, C., and Silva, R. (2017a). Counterfactual fairness. *Advances in neural information processing systems*, 30.
- Kusner, M. J., Loftus, J. R., Russell, C., and Silva, R. (2017b). Counterfactual fairness. In *Advances in Neural Information Processing Systems 30: Annual Conference on Neural Information Processing Systems 2017, December 4-9, 2017, Long Beach, CA, USA*, pages 4066–4076.
- Monteiro, M., Ribeiro, F. D. S., Pawlowski, N., Castro, D. C., and Glocker, B. (2023). Measuring axiomatic soundness of counterfactual image models.
- Munk, M. R., Kurmann, T., Márquez-Neila, P., Zinkernagel, M. S., Wolf, S., and Sznitman, R. (2021). Assessment of patient specific information in the wild on fundus photography and optical coherence tomography. *Scientific Reports*, 11(1):8621.
- Müller-Franzes, G., Niehues, J. M., Khader, F., Arasteh, S. T., Haarburger, C., Kuhl, C., Wang, T., Han, T., Nolte, T., Nebelung, S., Kather, J. N., and Truhn, D. (2023a). A multimodal comparison of latent denoising diffusion probabilistic models and generative adversarial networks for medical image synthesis. *Scientific Reports*, 13(12098).

- Müller-Franzes, G., Niehues, J. M., Khader, F., Arasteh, S. T., Haarburger, C., Kuhl, C., Wang, T., Han, T., Nolte, T., Nebelung, S., Kather, J. N., and Truhn, D. (2023b). A multimodal comparison of latent denoising diffusion probabilistic models and generative adversarial networks for medical image synthesis. *Scientific Reports*, 13(1).
- Navarrete-Dechent, C., Dusza, S. W., Liopyris, K., Marghoob, A. A., Halpern, A. C., and Marchetti, M. A. (2018). Automated dermatological diagnosis: Hype or reality? *Journal of Investigative Dermatology*, 138(10):1280.
- Newey, W. K. and Robins, J. R. (2018). Cross-fitting and fast remainder rates for semiparametric estimation.
- Nichol, A. and Dhariwal, P. (2021a). Improved denoising diffusion probabilistic models. *CoRR*, abs/2102.09672.
- Nichol, A. Q. and Dhariwal, P. (2021b). Improved denoising diffusion probabilistic models. In *Proceedings of ICML*, pages 8162–8171.
- Packhäuser, K., Folle, L., Thamm, F., and Maier, A. (2023). Generation of anonymous chest radiographs using latent diffusion models for training thoracic abnormality classification systems. In *20th IEEE International Symposium on Biomedical Imaging, ISBI 2023, Cartagena, Colombia, April 18-21, 2023*, pages 1–5. IEEE.
- Pandey, K., Mukherjee, A., Rai, P., and Kumar, A. (2021). Vaes meet diffusion models: Efficient and high-fidelity generation. In *Proceedings of NeurIPS Workshop on DGMs and Applications*.
- Pearl, J. (2000). *Causality: Models, Reasoning and Inference*. Cambridge University Press.
- Pearl, J. (2009). *Causality: Models, Reasoning and Inference*. Cambridge University Press.
- Peters, J., Janzing, D., and Schölkopf, B. (2017). *Elements of Causal Inference: Foundations and Learning Algorithms*. The MIT Press.
- Pinaya, W. H. L., Tudosi, P., Dafflon, J., Costa, P. F. D., Fernandez, V., Nachev, P., Ourselin, S., and Cardoso, M. J. (2022). Brain imaging generation with latent diffusion models. In *Deep Generative Models - Second MICCAI Workshop, DGM4MICCAI 2022, Held in Conjunction with MICCAI 2022, Singapore, September 22, 2022, Proceedings*, volume 13609 of *Lecture Notes in Computer Science*, pages 117–126. Springer.
- Pogodin, R., Deka, N., Li, Y., Sutherland, D. J., Veitch, V., and Gretton, A. (2023). Efficient conditionally invariant representation learning.
- Poplin, R., Varadarajan, A. V., Blumer, K., Liu, Y., McConnell, M. V., Corrado, G. S., Peng, L., and Webster, D. R. (2018). Prediction of cardiovascular risk factors from retinal fundus photographs via deep learning. *Nature Biomedical Engineering*, 2(3):158–164.
- Quinzan, F., Casolo, C., Muandet, K., Kilbertus, N., and Luo, Y. (2022). Learning counterfactually invariant predictors. *CoRR*, abs/2207.09768.
- Quinzan, F., Casolo, C., Muandet, K., Luo, Y., and Kilbertus, N. (2024). Learning counterfactually invariant predictors.
- Quinzan, F., Soleymani, A., Jaillet, P., Rojas, C. R., and Bauer, S. (2023). DRCFS: doubly robust causal feature selection. In *International Conference on Machine Learning, ICML 2023, 23-29 July 2023, Honolulu, Hawaii, USA*, volume 202 of *Proceedings of Machine Learning Research*, pages 28468–28491. PMLR.

- Rim, T. H., Lee, G., Kim, Y., Tham, Y.-C., Lee, C. J., Baik, S. J., Kim, Y. A., Yu, M., Deshmukh, M., Lee, B. K., Park, S., Kim, H. C., Sabayanagam, C., Ting, D. S. W., Wang, Y. X., Jonas, J. B., Kim, S. S., Wong, T. Y., and Cheng, C.-Y. (2020). Prediction of systemic biomarkers from retinal photographs: development and validation of deep-learning algorithms. *Lancet Digital Health*, 2(10):e526–e536.
- Rombach, R. and Blattmann, A. (2022). High-resolution image synthesis with latent diffusion models. In *CVPR*, pages 684–695.
- Rombach, R., Blattmann, A., Lorenz, D., Esser, P., and Ommer, B. (2022). High-resolution image synthesis with latent diffusion models. In *IEEE/CVF Conference on Computer Vision and Pattern Recognition, CVPR 2022, New Orleans, LA, USA, June 18–24, 2022*, pages 10674–10685. IEEE.
- Ronneberger, O., Fischer, P., and Brox, T. (2015a). U-net: Convolutional networks for biomedical image segmentation. In *Medical Image Computing and Computer-Assisted Intervention - MICCAI 2015 - 18th International Conference Munich, Germany, October 5 - 9, 2015, Proceedings, Part III*, volume 9351 of *Lecture Notes in Computer Science*, pages 234–241. Springer.
- Ronneberger, O., Fischer, P., and Brox, T. (2015b). U-net: Convolutional networks for biomedical image segmentation. *CoRR*, abs/1505.04597.
- Sarkar, R., Martin, C., Mattie, H., Gichoya, J. W., Stone, D. J., and Celi, L. A. (2021). Performance of intensive care unit severity scoring systems across different ethnicities in the usa: A retrospective observational study. *The Lancet Digital Health*, 3(4):e241–e249.
- Sehwag, V., Hazirbas, C., Gordo, A., Ozgenel, F., and Canton, C. (2022). Generating high fidelity data from low-density regions using diffusion models. In *Proceedings of CVPR*, pages 11492–11501.
- Seyyed-Kalantari, L., Zhang, H., McDermott, M. B. A., Chen, I. Y., and Ghassemi, M. (2021). Underdiagnosis bias of artificial intelligence algorithms applied to chest radiographs in under-served patient populations. *Nature Medicine*, 27(12):2176–2182.
- Siddique, N., Sidike, P., Elkin, C. P., and Devabhaktuni, V. K. (2021). U-net and its variants for medical image segmentation: A review of theory and applications. *IEEE Access*, 9:82031–82057.
- Simonyan, K. and Zisserman, A. (2015). Very deep convolutional networks for large-scale image recognition.
- Sohl-Dickstein, J. and Weiss, E. (2015). Deep unsupervised learning using nonequilibrium thermodynamics. In *ICML*.
- Sohl-Dickstein, J., Weiss, E., Maheswaranathan, N., and Ganguli, S. (2015). Deep unsupervised learning using non-equilibrium thermodynamics. In *Proceedings of ICML*, pages 2256–2265.
- Song, J., Meng, C., and Ermon, S. (2020). Denoising diffusion implicit models. *CoRR*, abs/2010.02502.
- Song, J., Meng, C., and Ermon, S. (2021). Denoising diffusion implicit models. In *Proceedings of ICLR*.
- Szegedy, C., Vanhoucke, V., Ioffe, S., Shlens, J., and Wojna, Z. (2015). Rethinking the inception architecture for computer vision.

- Veitch, V., D’Amour, A., Yadlowsky, S., and Eisenstein, J. (2021). Counterfactual invariance to spurious correlations in text classification. In *Advances in Neural Information Processing Systems 34: Annual Conference on Neural Information Processing Systems 2021, NeurIPS 2021, December 6-14, 2021, virtual*, pages 16196–16208.
- Williams, D. (1991). *Probability with Martingales*. Cambridge University Press.
- Yang, Y., Zhang, H., Gichoya, J., Katabi, D., and Ghassemi, M. (2024). The limits of fair medical imaging ai in real-world generalization. *Nature Medicine*, 30:2838–2848.
- Yi, P. H., Wei, J., Kim, T. K., Shin, J., Sair, H. I., Hui, F. K., Hager, G. D., and Lin, C. T. (2021). Radiology “forensics”: determination of age and sex from chest radiographs using deep learning. *emergency Radiology*, 28(5):949–954.
- Yuan, Z., Yan, Y., Sonka, M., and Yang, T. (2021). Large-scale robust deep AUC maximization: A new surrogate loss and empirical studies on medical image classification. In *2021 IEEE/CVF International Conference on Computer Vision, ICCV 2021, Montreal, QC, Canada, October 10-17, 2021*, pages 3020–3029. IEEE.

Appendix

A Structural Causal Models

A.1 Overview

Definition A.1 (Structural Causal Model (SCM), Definition 2.1 by Bongers et al. [2021]). A structural causal model (SCM) is defined as a tuple $\langle \mathbf{I}, \mathbf{J}, \mathbf{V}, \mathbf{U}, \mathbf{f}, \mathbb{P}_{\mathbf{U}} \rangle$ where: (i) \mathbf{I} represents a finite index set for endogenous variables; (ii) \mathbf{J} is a disjoint finite index set for exogenous variables; (iii) $\mathbf{V} = \prod_{i \in \mathbf{I}} V_i$ is the Cartesian product of the domains of endogenous variables, where each V_j is a standard measurable space; (iv) $\mathbf{U} = \prod_{j \in \mathbf{J}} U_j$ is the Cartesian product of the domains of exogenous variables, where each U_j is also a standard measurable space; (v) $\mathbf{f}: \mathbf{V} \times \mathbf{U} \rightarrow \mathbf{V}$ is a measurable function defining the causal mechanisms; (vi) $\mathbb{P}_{\mathbf{U}} = \prod_{j \in \mathbf{J}} \mathbb{P}_{U_j}$ is a product measure where \mathbb{P}_{U_j} is a probability measure on U_j for each $j \in \mathbf{J}$.

In structural causal models, the relationships among variables are captured through deterministic equations, which enable the modeling of cause-effect dynamics underlying the DGP using *structural equations*. For a spECAfic SCM $\langle \mathbf{I}, \mathbf{J}, \mathbf{V}, \mathbf{U}, \mathbf{f}, \mathbb{P}_{\mathbf{U}} \rangle$, a structural equation defines an endogenous random variable V_l through a measurable function of the form $V_l = f_{V_l}(\mathbf{V}, \mathbf{U})$ for all $l \in \mathbf{I}$. A *parent* $i \in \mathbf{I} \cup \mathbf{J}$ of l is an index such that no measurable function $g: \prod_{j \in \mathbf{I} \setminus i} V_j \times \mathbf{U} \rightarrow V_l$ exists with $f_{V_l} = g$ almost surely. Intuitively, each endogenous variable V_j is determined by its parents and the exogenous variables via the structural equations. A structural causal model as in Definition A.1 can be succinctly represented by a *causal graph*, a directed graph denoted by $\mathcal{G} = (\mathbf{I} \cup \mathbf{J}, \mathcal{E})$. The graph’s nodes correspond to all variable indices, and the edges are determined by the structural equations, i.e., $j \rightarrow l \in \mathcal{E}$ if and only if j is a parent of l . The variables in $\text{Pa}(V_l)$ are indexed by the parent nodes of l in the graph \mathcal{G} .

A.2 Interventions

The causal semantics of SCMs are defined through the concept of perfect interventions [Pearl, 2000]. For a given SCM as per Definition A.1, consider a variable $\mathbf{W} := \prod_{j \in \mathbf{I}'} V_j$ for some subset $\mathbf{I}' \subseteq \mathbf{I}$. Let $\mathbf{w} := \prod_{j \in \mathbf{I}'} v_j$ denote a point in its domain. A perfect intervention $\mathbf{W} \leftarrow \mathbf{w}$ entails substituting the structural equations $V_j = f_{V_j}(\mathbf{V}, \mathbf{U})$ with constant functions $V_j \equiv v_j$ for all $j \in \mathbf{I}'$. The variable $V_l | do(\mathbf{w})$ represents V_l after the intervention. This intervention induces a new probability distribution $\mathbb{P}(v_l | do(\mathbf{w}))$, referred to as the interventional distribution. It encodes the information: “Given that $\mathbf{W} = \mathbf{w}$ is observed, what would V_l be if $do(\mathbf{w})$ were performed, as opposed to the actual value taken by \mathbf{W} ?”

B Existing Notions of Counterfactual Invariance

In this section, we compare the definition of Counterfactual Invariance (CI) provided by Fawkes et al. [2022a], Kusner et al. [2017b], Quinzan et al. [2024] with Def. 4.1.

Almost Sure CI (a.s.-CI): Almost Sure CI (a.s.-CI), as defined by Fawkes et al. [2022a], requires that a variable Y remains exactly the same almost surely under any interventions on A . Formally, Y satisfies a.s.-CI with respect to A if it holds $Y | do(A = a) = Y | do(A = a')$ a.s. for all a, a' in the support of A . In contrast, Def. 4.1 focuses on the expected value of the predicted outcome \hat{Y} given an intervention on the attribute A while conditioning on the features $\mathbf{Z} = \mathbf{z}$. Thus, a.s.-CI is a stricter notion of invariance, as it requires exact equality almost surely, while the new definition allows for variations as long as the expected values remain the same.

CI for Functions (\mathcal{F} -CI): CI for Functions (\mathcal{F} -CI), as defined by Fawkes and Evans

[2023b] and Veitch et al. [2021], requires that the output of a function f : remains the same almost surely for any counterfactual states of the input X . Formally, f is counterfactually invariant if $f(X) | do(A = a) = f(X) | do(A = a')$ a.s. for all a, a' in the support of A . Def. 4.1 is similar in that it involves the function’s output remaining invariant under different interventions. However, it is less stringent, as it requires only the invariance of the *expected* values. Therefore, \mathcal{F} -CI requires exact equality in the outputs, while the new definition requires equality only in their expectations.

Distributional CI (\mathcal{D} -CI): Distributional CI (\mathcal{D} -CI), as defined by Fawkes and Evans [2023b], requires that the conditional probability distributions of a variable Y given a set of variables W remain the same under different interventions on A . Formally, Y satisfies \mathcal{D} -CI conditional on W with respect to A if it holds

$$P(Y = y | W = w, A = a, do(A = a)) = P(Y = y | W = w, A = a, do(A = a'))$$

for all a, a' in the support of A . Def. 4.1 is weaker. In fact, while both concepts address invariance under different interventions, the new definition focuses on the first moment (expectation) rather than the entire distribution.

CI in a Structural Causal Model (SCM): CI in a Structural Causal Model (SCM) as in Quinzan et al. [2024], as defined earlier, considers a variable Y invariant under different interventions on A , conditional on another set of variables W . The SCM-based definition is more general and can imply the new definition if applied to expectations rather than full distributions.

C Mutual Information Neural Estimation

Mutual Information Neural Estimation (MINE) is a framework designed to estimate the mutual information between random variables using neural networks [Belghazi et al., 2018]. Mutual information is a Shannon entropy-based metric that quantifies the dependency between two random variables, denoted as $I(X; Z)$. It measures the reduction in uncertainty about X given knowledge of Z , mathematically defined as $I(X; Z) := H(X) - H(X | Z)$, where $H(X)$ is the Shannon entropy of X , and $H(X | Z)$ is the conditional entropy of X given Z .

The mutual information can be expressed as the Kullback-Leibler (KL-) divergence $I(X, Z) = D_{\text{KL}}(P_{X,Z} \| P_X \otimes P_Z)$ between the joint distribution $P_{X,Z}$ and the product of the marginals $P_X \otimes P_Z$ as

$$D_{\text{KL}}(P_{X,Z} \| P_X \otimes P_Z) := \mathbb{E}_{P_{X,Z}} \left[\log \frac{P_{X,Z}}{P_X \otimes P_Z} \right].$$

The intuition behind this is that if the joint distribution $P_{X,Z}$ deviates significantly from the product of the marginals $P_X \otimes P_Z$, there is a strong dependency between X and Z . If X and Z are independent, the mutual information will vanish.

MINE leverages dual representations of the KL-divergence to estimate mutual information. One such representation is the Donsker-Varadhan duality [Donsker and Varadhan, 1983], which expresses the KL-divergence as $D_{\text{KL}}(P_{X,Z} \| P_X \otimes P_Z) = \sup_T \mathbb{E}_{P_{X,Z}}[T] - \log(\mathbb{E}_{P_X \otimes P_Z}[e^T])$, where T is any function for which the expected values are finite. This representation enables the construction of a lower bound for mutual information that can be optimized over a parameterized function space. Hence, we can parameterize the function T with a Neural Network T_θ , and optimize its parameters. The resulting estimate yields

$$I(P_{X,Z}; P_X \otimes P_Z) \leq \max_{\theta} \mathbb{E}_{P_{X,Z}}[T_\theta] - \log(\mathbb{E}_{P_X \otimes P_Z}[e^{T_\theta}]). \quad (6)$$

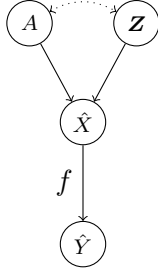


Figure 5: Causal structure for the DGP of the CLDM as in Fig. 1.

D Proof of Theorem 4.2

In order to prove Theorem 4.2, we use the well-known concept of valid adjustment set in causal inference. For a review on this notion and its properties we refer the reader to , e.g., Pearl [2009], Peters et al. [2017].

Definition D.1 (Valid Adjustment Set). Let \mathcal{G} be a causal graph and let A, \hat{Y} be disjoint (sets of) nodes in \mathcal{G} . A set of nodes \mathbf{Z} is a valid adjustment set for $\{A, \hat{Y}\}$, if (i) no element in \mathbf{Z} is a descendant of any node which lies on a proper causal path from A to \hat{Y} , in the graph obtained by removing from \mathcal{G} all incoming arrows into nodes in A ; (ii) \mathbf{Z} blocks all non-causal paths from A to \hat{Y} in \mathcal{G} .

Valid adjustment sets have the following important property.

Lemma D.2. *Let \mathbf{Z} be a valid adjustment set for $\{A, \hat{Y}\}$. Then, it holds $\hat{Y} \mid do(A = a) \perp A \mid \mathbf{Z}$, for all values a in the support of A .*

We now have all the tools to prove the following lemma.

Lemma D.3. *Consider the predicted outcome $\hat{Y} = f(\hat{X})$, with \hat{X} a r.v. generated by a CLDM as in Fig. 1. Then, it holds $\hat{Y} \mid do(A = a) \perp A \mid \mathbf{Z}$, for all possible values of a .*

Proof. Consider the generative process given by the CLDM as in Fig 1. In order to generate an image \hat{X} , we sample a representation vector $\mathbf{Z} = \mathbf{z}_T$ according to a Gaussian prior, and denoise this representation vector using a conditioning label $A = a$. Then, the predicted label of interest \hat{Y} is given as $\hat{Y} = f(\hat{X})$, for a base classifier f . This generative process can be visualized with a causal graph as in Fig. 5. In this graph, the variable \mathbf{Z} is a valid adjustment set for $\{A, \hat{Y}\}$. Hence, the claim follows by Lemma D.2. \square

We can now prove Theorem 4.2.

Proof of Theorem 4.2. First of all, note that by the conditional ignorability assumption we have that $\mathbb{E}[\hat{Y} \mid do(A = a), \mathbf{Z} = \mathbf{z}] = \mathbb{E}[\hat{Y} \mid A = a, \mathbf{Z} = \mathbf{z}]$ for all a . Hence, a model $f(X)$ is counterfactually invariant with respect to the attribute A if, for any input X with features $\mathbf{Z} = \mathbf{z}$, the predicted outcome $\hat{Y} := f(X)$ satisfies $\mathbb{E}[\hat{Y} \mid A = a, \mathbf{Z} = \mathbf{z}] = \mathbb{E}[\hat{Y} \mid A = a', \mathbf{Z} = \mathbf{z}]$. Equivalently, a model is counterfactually invariant if it holds

$$\mathbb{E} \left[\left(\mathbb{E}[\hat{Y} \mid A, \mathbf{Z}] - \mathbb{E}[\hat{Y} \mid \mathbf{Z}] \right)^2 \right] = 0,$$

where the expected value is taken on A and \mathbf{Z} . By the tower property of the expectation [Williams, 1991] that

$$\begin{aligned}
\mathbb{E} \left[\left(\mathbb{E} [\hat{Y} | A, \mathbf{Z}] - \mathbb{E} [\hat{Y} | \mathbf{Z}] \right)^2 \right] &= \mathbb{E} \left[\mathbb{E} \left[\left(\mathbb{E} [\hat{Y} | A, \mathbf{Z}] - \mathbb{E} [\hat{Y} | \mathbf{Z}] \right)^2 \mid \mathbf{Z} \right] \right] \\
&= \mathbb{E} \left[\mathbb{E} \left[\left(\mathbb{E} [\hat{Y} | A, \mathbf{Z}]^2 - \mathbb{E} [\hat{Y} | A, \mathbf{Z}] \mathbb{E} [Y | \mathbf{Z}] \right) \mid \mathbf{Z} \right] \right] \\
&= \mathbb{E} \left[\mathbb{E} [\hat{Y} | A, \mathbf{Z}]^2 \right] - \mathbb{E} \left[\mathbb{E} [\hat{Y} | A, \mathbf{Z}] \mathbb{E} [\hat{Y} | \mathbf{Z}] \mid \mathbf{Z} \right] \\
&= \mathbb{E} \left[\mathbb{E} [\hat{Y} | A, \mathbf{Z}]^2 \right] - \mathbb{E} \left[\mathbb{E} [\hat{Y} | \mathbf{Z}]^2 \right] \\
&= \mathbb{E} [\hat{Y} \mathbb{E} [\hat{Y} | A, \mathbf{Z}]] - \mathbb{E} [\hat{Y} \mathbb{E} [\hat{Y} | \mathbf{Z}]].
\end{aligned}$$

Hence, a predictor $f(X)$ is counterfactually invariant iff. it holds $\mathbb{E} [\hat{Y} \mathbb{E} [\hat{Y} | A, \mathbf{Z}]] = \mathbb{E} [\hat{Y} \mathbb{E} [\hat{Y} | \mathbf{Z}]]$ as claimed. \square

E ECA Alignment

The fact that $\mathbb{E}[\hat{Y} | do(A = a), \mathbf{Z} = \mathbf{z}] = \mathbb{E}[\hat{Y} | A = a, \mathbf{Z} = \mathbf{z}]$ follows directly from Lemma D.3.

F Datasets Description

F.1 Synthetic Datasets

We consider six synthetic datasets, namely, linear, quadratic, exponential, interactive, log-exponent, and sin. Each synthetic datasets consist of features $\mathbf{Z} = \{Z_0, \dots, Z_n\}$ together with a protected feature A , as well as observations X and corresponding labels Y . The DGP is described by the following equations:

$$\begin{cases} A \sim \text{BERNOULLI}(0.3) \\ Z_t = M_t Z_{t+1} A + N_t Z_{t+1} (1 - A) + \xi_t, \quad t = 0, 1, \dots, n-1 \\ X = M_X Z_0 + r + \epsilon_X \\ Y \sim \text{BERNOULLI}(\text{SIGMOID}(f_Y(Z_n))) \end{cases}$$

In this data generating process, parameters $M_i, N_i, M_X \in \mathbb{R}^{k \times k}$ are transformation matrices; $r \in \mathbb{R}^k$ is a parameter representing the bias; $\xi_i, \epsilon_X \sim \mathcal{N}(0, \sigma^2)$ are random errors. f_Y is a transformation layer that adds nonlinearity before the sigmoid activation. For each transformation, we use a different random realization of the parameters, thereby generating different synthetic datasets. We apply one linear transformation and five nonlinear transformations for f_Y :

- linear: $f_Y(Z_n) = \omega_Y \cdot Z_n + b_Y$, with $\omega_Y \sim \mathcal{N}(\mathbf{0}, I)$ and $b_Y \sim \mathcal{N}(0, 1)$.
- quadratic: $f_Y(Z_n) = \omega_Y \cdot (Z_n)^2 + b_Y$, with $\omega_Y \sim \mathcal{N}(\mathbf{0}, 4I)$ and $b_Y \sim \mathcal{N}(20, 1)$.
- exponential: $f_Y(Z_n) = \omega_Y \cdot e^{Z_n} + b_Y$, with $\omega_Y \sim \mathcal{N}(\mathbf{0}, I)$ and $b_Y \sim \mathcal{N}(10, 1)$.
- interactive: $f_Y(Z_n) = \sum_{i \neq j} \omega_Y^{i,j} \cdot Z_n^i \cdot Z_n^j + b_Y$, with $\omega_Y^{i,j} \sim \mathcal{N}(0, 1)$ and $b_Y \sim \mathcal{N}(0, 1)$.
- log-exponent: $f_Y(Z_n) = \log(\exp(\omega_Y \cdot Z_n) + b_Y)$, with $\omega_Y \sim \mathcal{N}(0, I)$ and $b_Y \sim \mathcal{N}(5, 1)$.
- sin: $f_Y(Z_n) = \omega_Y \cdot \sin(Z_n) + b_Y$, with $\omega_Y \sim \mathcal{N}(\mathbf{0}, I)$ and $b_Y \sim \mathcal{N}(2, 1)$.

Here, ω_Y and b_Y are fixed model parameters during the generation process. During the simulation, we take the following values on the hyperparameters $T = 3, k = 32, \sigma = 0.01$. The SCM's parameter M_t, N_t are random matrix whose elements are sampled from uniform distribution $[-10, 10]$. The initial state $Z_n \sim \mathcal{N}(0, I_k)$.

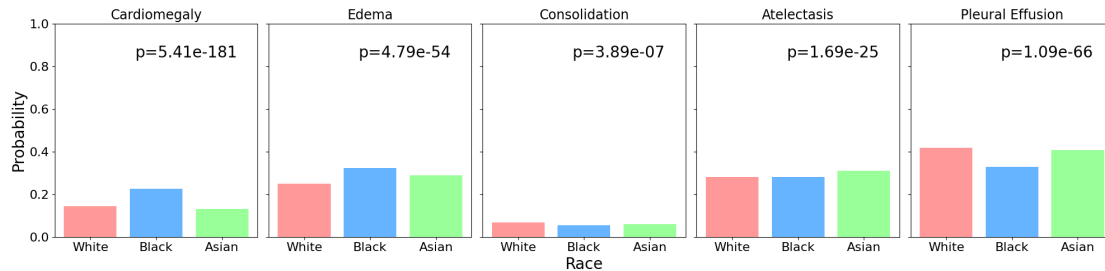


Figure 6: **Association between race and diseases in the CHEXPert dataset.** This plot visualizes the probability of five different diseases across three racial groups: White, Black, and Asian. Each subplot represents a spECafic disease, with three bars indicating the average probability of the disease occurring within each racial group. Additionally, the p-values from the chi-square test show whether the correlation between race and disease is significant.

F.2 The CHEXPert Dataset

CHEXPert is a large dataset that contains 224,316 chest radiographs of 65,240 patients [Irvin et al., 2019]. Images are labeled for the presence of common chest radiographic observations. For simplicity, following previous work [Yuan et al., 2021], we only consider five of these observations in these experiments, namely Cardiomegaly, Edema, Consolidation, Atelectasis, and Pleural Effusion. Images in the CHEXPert dataset are paired with demographic labels for the patients, including the self-reported race. In this dataset there are 55.5% patients labeled as “male”, and 55.5% patients labeled as “female”. In this dataset, 4.8% patients are labeled as “black”, 10.8% patients are labeled as “asian”, 56.2% patients are labeled as “white”, and 28.2% of the patients are labeled as “unknown”. In our experiments, the CHEXPert dataset is filtered by the view (only frontal chest image) and races (restricted to “black”, “white” and “asian”).

Association between disease and self-reported race. In this section, we investigate whether there is a correlation between race and disease. To do this we compute the conditional probability of having a disease given the racial attribute. To check if there is an dependency, we apply the chi-square test. The result is shown in Figure 6, indicating that in the CheXpert dataset, the racial attribute is significantly correlated with all the five inspected diseases. This association is particularly strong for cardiomegaly, edema, and pleural effusion.

F.3 The MIMIC-CXR Dataset

MIMIC-CXR [Johnson et al., 2019a,b] is a large publicly available datasets consisting of chest x-ray images and associated radiological reports. Same as the Chexpert dataset, labels are extracted from the report and 5 out of 14 are used for our research, namely Cardiomegaly, Edema, Consolidation, Atelectasis and Pleural Effusion. Demographic labels of the patients are also available, such as sex and self-reported race, providing an identical research setting as that of the Chexpert. In the dataset, %52.17 patients are labeled as "male" and %47.83 are labeled as "female". In terms of self-reported race, 3.2% are labeled as "asian", 18.5% are labeled as "black" and 67.6% are labeled as "white". In the research, we restrict the race to only black, white and asian and further filter the dataset by view to include only frontal images.

Association between disease and self-reported race. Similar to the CHEXPert dataset, there is a significant correlation observed in some of the disease labels. However, the pattern is different with that of CHEXPert’s correlation 6. For MIMIC-CXR the correlation are spECafically stronger for Atelectasis and Pleural Effusion. We will show that this leads to different results.

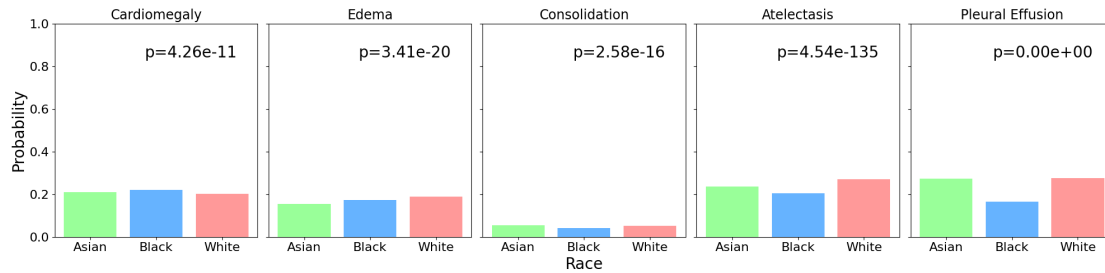


Figure 7: **Association between race and diseases in the MIMIC-CXR dataset.** This plot visualizes the probability of five different diseases across three (self-reported) racial groups: White, Black, and Asian. Each subplot represents a spECAFic disease, with three bars indicating the average probability of the disease occurring within each group.

G Base Classifiers for Experimental Comparison

G.1 Base Classifiers for the Synthetic Datasets

In our experiment the examined objects are classifiers that predicts Y given X . We create a model pool with 100 statistical learning models that includes various models. We initially consider 10 types of models as in Tab. 1. Then, we initialize and train this model under 10 different random scenarios, which are realized through setting the random seed in scikit-learn package. This results in 100 different models.

Model	Hyperparameters
Support Vector Classifier (linear kernel)	$C=1.0$, $loss='squared_hinge'$, $dual=True$, $tol=1e-4$
Support Vector Classifier (RBF Kernel)	$C=1.0$, $kernel='rbf'$, $gamma='scale'$
Support Vector Classifier (Polynomial Kernel)	$C=1.0$, $kernel='poly'$, $degree=3$, $gamma='scale'$
LogisticRegression	$penalty='l2'$, $C=1.0$, $solver='lbfgs'$, $max_iter=100$
DECAstionTreeClassifier	$criterion='gini'$, $splitter='best'$, $max_depth=None$
RandomForestClassifier	$n_estimators=50$, $criterion='gini'$, $max_features='auto'$
GradientBoostingClassifier	$n_estimators=100$, $learning_rate=0.1$, $max_depth=3$
DECAstionTreeClassifier ($max_depth=5$)	$criterion='gini'$, $splitter='best'$, $max_depth=5$
MLPClassifier (16, 8, 4)	$hidden_layer_sizes=(16, 8, 4)$, $activation='relu'$, $solver='adam'$, $max_iter=500$
MLPClassifier (16, 4)	$hidden_layer_sizes=(16, 4)$, $activation='relu'$, $solver='adam'$, $max_iter=500$

Table 1: Machine learning models and their hyperparameters used for classification on the synthetic datasets

G.2 Base Classifiers for cheXpert and MIMIC-CXR

Model architectures. Same setting is applied to Chexpert and MIMIC-CXR dataset. The diagnosis models, namely the disease classifiers, are trained to predict five diseases simultaneously. The five diseases are cardiomegaly, edema, consolidation and pleural effusion. All the models have the same high level structure: the image is processed through a backbone

to produce high-level feature maps. The feature map then goes through a global average pooling operation, reducing the spatial dimension to (1, 1). Then for each of the five labels, dropout and batch normalization are applied before passing through a label-specific 1×1 convolutional classifier to obtain the logits. We consider three types of CNN models, namely DensenetHuang et al. [2016], VGG Simonyan and Zisserman [2015] and inception-V3Szegedy et al. [2015]. For each type of backbone we select multiple variations. For Densenet, we select Densenet 121, Densenet 169 and Densenet 201. For VGG, we select VGG13, VGG13+BN, VGG16, VGG16+BN, VGG19, VGG19+BN. For VGG family’s models, '+BN' means that an additional batch normalization is applied in each convolution layer.

Training details. The training, validation and test set are splitted in the same way as we did in training the CLDM for Chexpert and MIMIC-CXR respectively. Images are resized to 256×256 with the pixel value scaled to $[-1, 1]$. For each model, we download the pretrained backbone from torchvision and then train the full model with a batchsize of 64 and a learning rate of $1e^{-4}$ for 20 epochs. The loss is computed as the sum of binary cross entropy loss of five labels. We optimize the parameters using the Adam optimizer.

Performance across demographic groups. we report the performance of the diagnostic models by describing the ROCAUC scores. Results are shown in Table 2 (CheXpert) and Table 3 (MIMIC-CXR).

Model	Race	Cardiomegaly	Edema	Consolidation	Atelectasis	Pleural Effusion
densenet121	Black	0.820	0.710	0.961	0.770	0.830
	White	0.880	0.780	0.943	0.720	0.870
	Asian	0.810	0.730	0.925	0.770	0.850
densenet169	Black	0.870	0.870	0.950	0.830	0.850
	White	0.953	0.872	0.941	0.810	0.830
	Asian	0.892	0.880	0.931	0.840	0.850
densenet201	Black	0.840	0.850	0.944	0.800	0.900
	White	0.940	0.871	0.950	0.800	0.870
	Asian	0.881	0.884	0.926	0.820	0.860
VGG13	Black	0.860	0.850	0.961	0.830	0.890
	White	0.930	0.900	0.930	0.750	0.870
	Asian	0.880	0.949	0.918	0.790	0.830
VGG13+BN	Black	0.850	0.830	0.963	0.810	0.900
	White	0.890	0.820	0.931	0.810	0.910
	Asian	0.860	0.830	0.926	0.850	0.930
VGG16	Black	0.830	0.860	0.964	0.790	0.900
	White	0.890	0.850	0.960	0.800	0.860
	Asian	0.860	0.870	0.926	0.760	0.850
VGG16+BN	Black	0.820	0.870	0.950	0.840	0.880
	White	0.900	0.920	0.921	0.820	0.860
	Asian	0.870	0.910	0.911	0.840	0.870
VGG19	Black	0.870	0.850	0.971	0.840	0.830
	White	0.940	0.910	0.930	0.810	0.810
	Asian	0.890	0.920	0.930	0.850	0.830
VGG19+BN	Black	0.840	0.870	0.951	0.810	0.900
	White	0.900	0.920	0.940	0.810	0.870
	Asian	0.870	0.920	0.928	0.800	0.830
Inception V3	Black	0.830	0.850	0.931	0.840	0.910
	White	0.890	0.860	0.940	0.790	0.870
	Asian	0.850	0.891	0.926	0.820	0.840

Table 2: ROC AUC Scores of 10 classification models for five diseases across demographic groups on the Chexpert dataset

Model	Race	Cardiomegaly	Edema	Consolidation	Atelectasis	Pleural Effusion
densenet121	Black	0.792	0.747	0.962	0.825	0.853
	White	0.854	0.819	0.944	0.775	0.887
	Asian	0.780	0.754	0.928	0.830	0.864
densenet169	Black	0.844	0.915	0.949	0.875	0.873
	White	0.926	0.915	0.939	0.862	0.857
	Asian	0.860	0.916	0.927	0.900	0.875
densenet201	Black	0.820	0.896	0.944	0.852	0.918
	White	0.912	0.913	0.951	0.861	0.898
	Asian	0.850	0.930	0.926	0.875	0.875
VGG13	Black	0.832	0.892	0.960	0.872	0.905
	White	0.898	0.946	0.931	0.810	0.898
	Asian	0.852	0.990	0.917	0.854	0.863
VGG13+BN	Black	0.821	0.872	0.964	0.865	0.916
	White	0.857	0.867	0.930	0.869	0.943
	Asian	0.831	0.871	0.926	0.898	0.968
VGG16	Black	0.806	0.896	0.965	0.851	0.920
	White	0.853	0.888	0.960	0.865	0.897
	Asian	0.826	0.905	0.928	0.822	0.868
VGG16+BN	Black	0.792	0.914	0.949	0.887	0.897
	White	0.872	0.966	0.920	0.887	0.897
	Asian	0.847	0.952	0.913	0.877	0.892
VGG19	Black	0.841	0.898	0.970	0.887	0.858
	White	0.912	0.957	0.932	0.862	0.856
	Asian	0.861	0.967	0.930	0.896	0.854
VGG19+BN	Black	0.818	0.911	0.949	0.857	0.916
	White	0.871	0.960	0.939	0.864	0.902
	Asian	0.841	0.961	0.930	0.877	0.857
Inception V3	Black	0.806	0.894	0.930	0.908	0.931
	White	0.861	0.902	0.941	0.854	0.911
	Asian	0.817	0.926	0.927	0.870	0.867

Table 3: ROC AUC Scores of 10 classification models for five diseases across demographic groups on MIMIC-CXR

H Implementation of Alg. 1

H.1 Implementation Details of the CLDM

Model architecture. The CLDM used in Alg. 1 consists of two components, the outside structure VAE and the inner structure diffusion model. The encoder is constructed as a series of convolutional layers and downsampling modules, which progressively reduce the spatial dimensions while capturing essential features from the input data. The decoder, on the other hand, consists of convolutional layers and upsampling modules, designed to reconstruct the original data from the latent representation. To enhance the model’s performance, attention mechanisms and skip connections are employed. The DDPM uses U-net as the noise estimator $\epsilon_\theta(\mathbf{z}_t, t, a)$ to denoise the latent space. The U-net is further augmented by a cross-attention mechanism to enable layer propagation with conditioned label. Technically, we adopt the classic archilatent diffusion tecture used for medical images [Dhariwal and Nichol \[2021b\]](#).

Training details. The outside VAE structure and the diffusion model inner structure are trained in two successive phases. In the first phase, the VAE is trained to encode a $256 \times 256 \times 1$ image into a $32 \times 32 \times 8$ latent representation and then decode it back into the original image space. Here the number of channels of the latent code adopts the strategy in [Müller-Franzes et al. \[2023b\]](#) which shows good performance. A multi-resolution loss function, combined with KL-regularization, is used as the training objective. In the second phase, the VAE is frozen, and the input image is encoded into the latent space by the encoder. Random noise is then sampled and used to diffuse the noised latent vector over 1000 steps. The U-Net [Ronneberger et al. \[2015b\]](#) is subsequently trained to predict the noise from the diffused sample, following the standard training procedure of the diffusion model. During sampling, the diffusion model strategy [Song et al. \[2020\]](#) is applied to accelerate the iterative process.

Variance control. For diffusion models, the hyperparameter β_t , $\alpha_t = 1 - \beta_t$ and the number of steps T controls the noise’s variance during the forward process, where data is gradually corrupted by adding Gaussian noise. β_t governs how much noise is added. In settings where the goal is to generate diverse images, the number of steps and β_t are usually set to 1000 and a linear interpolation between 0.001 to 0.01. In the counterfactual image generation, however, large β and T could lead to excessive variance in the generated images. To overcome this problem, in our analysis we use a variance reduction technique. Empirical studies [Nichol and Dhariwal \[2021a\]](#) show that steps between 50 to 500 can still produce high-quality images with reduced variance. Therefore in our task, we actively reduce β to 20% and T to 250 to fit our counterfactual demand. Experiments show that diffusion models achieves lower sample variance without significantly compromising the quality of the generated images.

H.2 Implementation Details of MINE

Model architectures. MINE is uses two functions, namely a non-linear transformation $\phi_{\lambda,\delta}(\mathbf{z}_0)$, and a Neural Network T_θ as in (4).

The non-linear transformation $\phi_{\lambda,\delta}(\mathbf{z}_0)$ is of the form

$$\phi_{\lambda,\delta}(\mathbf{z}_0) = \mathbf{z}_0 + \lambda \frac{m_\delta(\mathbf{z}_0)}{\|m_\delta(\mathbf{z}_0)\|}$$

This transformation is spECAFied by a perturbation network $m_\delta(\mathbf{z}_0)$. Since the perturbation ought to have the same shape of the input \mathbf{z}_0 , we adopt a U-shaped CNN architecture which is similar to the U-net. The network details are described in Table 4. To model the Neural Network T_θ , we use a CNN that is similar to the architecture of ResNet-18. The categorical input a is one-hot encoded into an vector $\text{Emb}(a)$ with shape $(32, 32, 2)$ and then concatenated with the latent representation \mathbf{z}_0 . The concatenated tensor is then input into the CNN

Table 4: Architecture of m_δ

Layer/Block	Module	Output Shape
Input	Input Tensor	(32, 32, 8)
Conv Block 1	Conv2D(16, 3x3) + ReLU BatchNorm Conv2D(16, 3x3) + ReLU BatchNorm MaxPooling(2x2)	(16, 16, 16)
Conv Block 2	Conv2D(32, 3x3) + ReLU BatchNorm Conv2D(32, 3x3) + ReLU BatchNorm MaxPooling(2x2)	(8, 8, 32)
Conv Block 3	Conv2D(64, 3x3) + ReLU BatchNorm Conv2D(64, 3x3) + ReLU BatchNorm MaxPooling(2x2)	(4, 4, 64)
Upsample Block 1	Upsample(2x2) Conv2D(32, 3x3) + ReLU BatchNorm Conv2D(32, 3x3) + ReLU BatchNorm	(8, 8, 32)
Upsample Block 2	Upsample(2x2) Conv2D(16, 3x3) + ReLU BatchNorm Conv2D(16, 3x3) + ReLU BatchNorm	(16, 16, 16)
Upsample Block 3	Upsample(2x2) Conv2D(8, 3x3) + ReLU BatchNorm Conv2D(8, 3x3) + ReLU BatchNorm	(32, 32, 8)
Final Output	Output Tensor	(32, 32, 8)

described in Table 5.

Training details. The objective function of the combined training of the two networks $\phi_{\lambda,\delta}$ and T_θ is a min-max problem as in (4). The optimization procedure for the problem in (4) is an alternative strategy that jointly maximizes the parameters θ and δ . This training procedure is iterated on CHEXPRT and MIMIC-CXR separately, using the same training set as the latent diffusion model in the CLDM. We used the Adam optimizer to update parameters of both networks, with an initial learning rate of $1e-4$ and weight decay of $1e-5$. The batch size was set to 64, and gradient clipping was applied with a maximum norm of 1.0. The hyperparameter λ is set to $1e-3$, using random search. The Mutual information estimator was updated for five iterations per training step, followed by one update of the perturbation network.

Layer/Block	Module	Output Shape
Input	Input Tensor = Concat($z_0, Emb(a)$)	(32, 32, 10)
Conv1	Conv2D(10, 64, 3x3, stride=1, padding=1) BatchNorm ReLU	(32, 32, 64)
Layer 1	2 x Residual Block (Conv2D(64, 64, 3x3, stride=1) BatchNorm ReLU)	(32, 32, 64)
Layer 2	2 x Residual Block (Conv2D(64, 128, 3x3, stride=2) BatchNorm ReLU)	(16, 16, 128)
Layer 3	2 x Residual Block (Conv2D(128, 256, 3x3, stride=2) BatchNorm ReLU)	(8, 8, 256)
Layer 4	2 x Residual Block (Conv2D(256, 512, 3x3, stride=2) BatchNorm ReLU)	(4, 4, 512)
Global Avg Pool	AdaptiveAvgPool2d(1x1)	(1, 1, 512)
Fully Connected	Linear(512, 1)	(1, 1)
Final Output	Real Number Output	(1)

Table 5: Network Architecture for Mutual information estimation T

I Experiments on Image Generation

We provide additional experiments to evaluate the quality of the images generated by a CLDM with disentangled representations as in Alg. 1. In this section, we use the acronym DLDM (Disentangled Latent Diffusion Model) to denote a CLDM with disentangled representations.

Evaluation Metrics. We consider two evaluation metrics:

- (FID score) The Fréchet Inception Distance (FID) evaluates the statistical similarity of extracted features from two sets of images. Hence it can be used to measure the quality of the counterfactual images to see whether they maintain the natural characteristics.
- (Composition) This metric is the reconstruction error between observed images and re-generated images with null intervention, i.e., the conditional attribute used to generate the image is the same as in the original image. Here, the reconstruction error is measured by L^1 -image distance.
- (Effectiveness Accuracy) This metric measures to which extent the CLDM generates images that are consistent with the conditioning labels. Effectiveness Accuracy is the proportion of the predicted racial labels that are equal to the racial labels used during generation. Since the effectiveness accuracy cannot be observed directly, we use a classifier to detect the conditioning label taken from Banerjee et al. [2021]. This classifier is a standard ResNet-34 [He et al., 2015]. We refer the reader to Tab. 6 for the performance of this classifier.

Baselines. We consider two baselines for experimental comparison. First, we consider

Table 6: ROC AUC score of the protected attribute predictor.

	Black	White	Asian	Unknown
CheXpert	$0.973 \pm 2.0e-3$	$0.980 \pm 3.5e-3$	$0.975 \pm 1.5e-3$	$0.943 \pm 5.2e-3$
MIMIC-CXR	$0.975 \pm 3.1e-3$	$0.981 \pm 1.2e-3$	$0.980 \pm 1.5e-3$	$0.940 \pm 4.7e-3$

β -VAE, a conditional β variational auto-encoder with $\beta = 0, 1, 10$ [Higgins et al., 2017, Kingma and Welling, 2014, Monteiro et al., 2023]. Then, we consider a standard conditional latent diffusion model (CLDM) as described in Sec. 3.2.

Results. The results are displayed in Table 7-Tab. 11. Overall we see significant improvements in the counterfactual effectiveness and the FID scores for DLDM.

Table 7: Composition (reconstruction error) on the CHEXPert test dataset.

Model	Composition (L^1) \downarrow		
	$do(A = \text{black})$	$do(A = \text{asian})$	$do(A = \text{white})$
VAE ($\beta = 0$)	$251.4_{\pm 12.6}$	$242.8_{\pm 14.1}$	$248.7_{\pm 10.9}$
VAE ($\beta = 1$)	$241.8_{\pm 11.2}$	$230.4_{\pm 10.5}$	$238.5_{\pm 12.0}$
VAE ($\beta = 10$)	$275.6_{\pm 15.8}$	$268.2_{\pm 13.9}$	$271.9_{\pm 14.3}$
CLDM	$810.5_{\pm 41.3}$	$789.8_{\pm 38.5}$	$798.2_{\pm 39.7}$
DLDM	$340.2_{\pm 26.9}$	$320.8_{\pm 28.1}$	$330.5_{\pm 27.3}$

Table 8: Effectiveness Accuracy on the CHEXPert test dataset.

Model	Effectiveness Accuracy (%) \uparrow		
	$do(A = \text{black})$	$do(A = \text{asian})$	$do(A = \text{white})$
VAE ($\beta = 0$)	78.2	82.0	84.5
VAE ($\beta = 1$)	81.2	85.3	87.4
VAE ($\beta = 10$)	76.8	80.1	82.2
CLDM	83.5	87.2	89.1
DLDM	88.7	91.8	93.3

Table 9: Composition (reconstruction error) of the image generation on the MIMIC-CXR test dataset.

Model	Composition (L^1) \downarrow		
	$do(A = \text{black})$	$do(A = \text{asian})$	$do(A = \text{white})$
VAE ($\beta = 0$)	$255.3_{\pm 13.2}$	$246.7_{\pm 15.0}$	$243.9_{\pm 11.5}$
VAE ($\beta = 1$)	$245.6_{\pm 12.0}$	$234.1_{\pm 11.8}$	$232.7_{\pm 13.5}$
VAE ($\beta = 10$)	$280.2_{\pm 16.5}$	$272.9_{\pm 14.7}$	$269.1_{\pm 15.1}$
CLDM	$815.9_{\pm 42.5}$	$798.3_{\pm 39.8}$	$793.6_{\pm 40.9}$
DLDM	$346.1_{\pm 27.5}$	$324.4_{\pm 28.8}$	$322.3_{\pm 27.9}$

Table 10: Effectiveness Accuracy on the MIMIC-CXR test dataset.

Model	Effectiveness Accuracy (%) \uparrow		
	$do(A = black)$	$do(A = asian)$	$do(A = white)$
VAE ($\beta = 0$)	79.0	83.2	85.9
VAE ($\beta = 1$)	82.1	86.5	88.2
VAE ($\beta = 10$)	78.0	81.5	83.4
CLDM	84.1	87.8	89.6
DLDM	89.2	92.0	93.7

Table 11: FID score of the generated counterfactual images on MIMIC and CheXpert dataset

Model / Dataset	CheXpert	MIMIC-CXR
VAE ($\beta = 0$)	24.23	26.33
VAE ($\beta = 1$)	23.92	26.92
VAE ($\beta = 10$)	25.10	27.22
CLDM	22.14	26.10
DLDM	21.79	25.89

I.1 Evaluate CI of diagnosis models

The goal of this set of experiments is to better understand to which extent the racial attributes influence the predictions of a given diagnostic model. We choose the Densenet121 classifier [Huang et al., 2016] from our diagnosis model pool as an example. For this model, we evaluate the predictions for five diseases, namely “pleural effusion”, “cardiomegaly”, “consolidation”, “atelectasis”.

Datasets description. In this set of experiments, we consider both the CHEXPert dataset and the MIMIC-CXR dataset.

Evaluation. The evaluation uses counterfactual analysis and statistical testing. Counterfactual images are generated by intervening on the racial attribute of each test image (e.g., changing the observed race from White to Black or Asian). These counterfactual images, alongside the original ones, are fed into the classifiers to compare predicted probabilities. Scatter plots are created to visualize the relationship between predictions for original and counterfactual images, with deviations from the $y = x$ reference line indicating potential racial influence.

Results. The results for CHEXPert are displayed in Fig. 8-12. Furthermore, Table 12-13 summarizes the paired t-test results for various diagnosis models. For cardiomegaly, edema and pleural effusion, most models show significant p -values, indicating a lack of CI. Whereas for consolidation, most models, such as Densenet 121 or VGG13+BN shows non-significant results ($p > 0.05$), exhibiting CI. However no model our tested pool is universally invariant across all the diseases, which suggests that models trained on pure observed dataset with a classic norm is intrinsically non-robust to such changes.

Result of the CIT-LR on MIMIC-CXR Result of the paired t-tests on CHEXPert and MIMIC-CXR are shown in Table 12-13. For cardiomegaly, edema and pleural effusion, most models show significant p -values, indicating a lack of CI. Whereas for consolidation, most models, such as Densenet 121 or VGG13+BN shows non-significant results ($p > 0.05$), exhibiting CI. However no model our tested pool is universally invariant across all the diseases, which suggests that models trained on pure observed dataset with a classic norm is intrinsically non-robust to such changes.

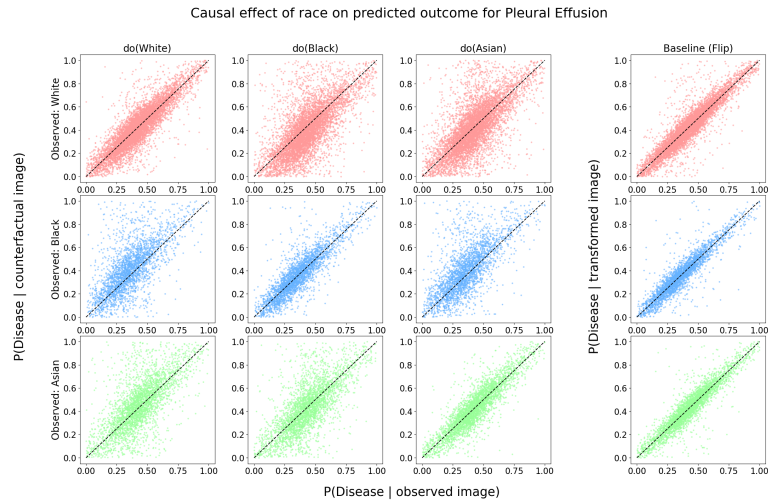


Figure 8: **Impact of the Protected Attribute on Disease Prediction using Counterfactual Images.** The scatter plots compare the predicted probability of pleural effusion for the original image (x-axis) and the generated image (y-axis), under different conditioning labels. The rows represent the observed race of the image, and the columns show the conditioning racial label, with the last column representing a baseline transformation (horizontal flip). The dashed diagonal line represents equal predictions for the original and counterfactual images.

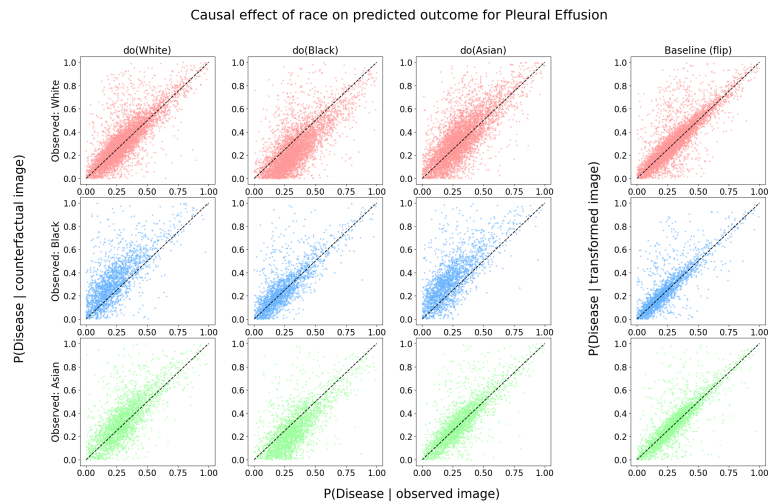


Figure 9: **Impact of the Protected Attribute on Disease Prediction using Counterfactual Images.** The scatter plots compare the predicted probability of pleural effusion for the original image (x-axis) and the generated image (y-axis), under different conditioning labels. The rows represent the observed race of the image, and the columns show the conditioning racial label, with the last column representing a baseline transformation (horizontal flip). The dashed diagonal line represents equal predictions for the original and counterfactual images.

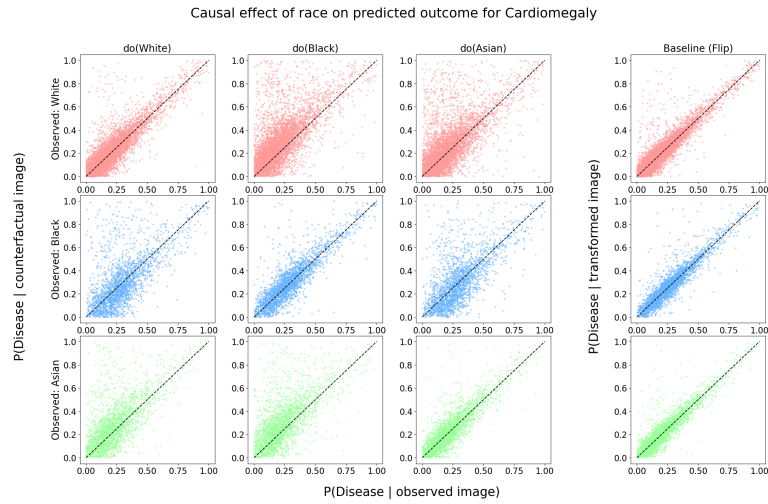


Figure 10: **Impact of the Protected Attribute on Cardiomegaly Prediction using Counterfactual Images.** The scatter plots compare the predicted probability of pleural effusion for the original image (x-axis) and the generated image (y-axis), under different conditioning labels. The rows represent the observed race of the image, and the columns show the conditioning racial label, with the last column representing a baseline transformation (horizontal flip). The dashed diagonal line represents equal predictions for the original and counterfactual images.

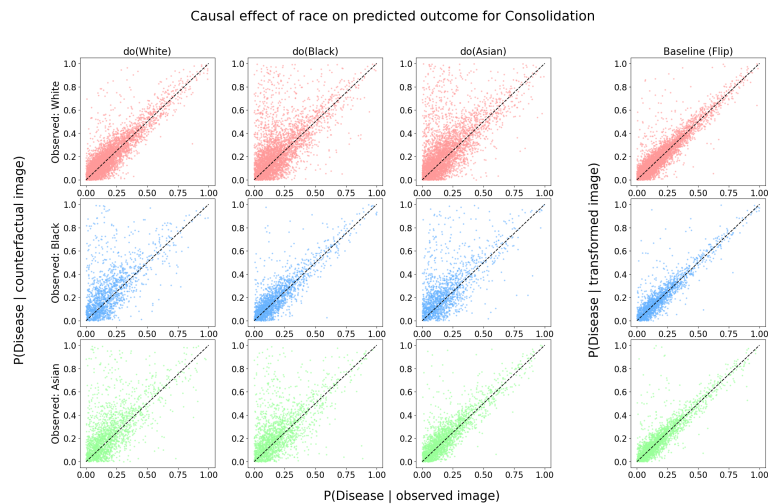


Figure 11: **Impact of the Protected Attribute on Consolidation Prediction using Counterfactual Images.** Results suggest that when the intervened race is different with the observed race, the predicted outcome has a bias, indicating causal effect of race on the predicted outcome learned by the predictor.

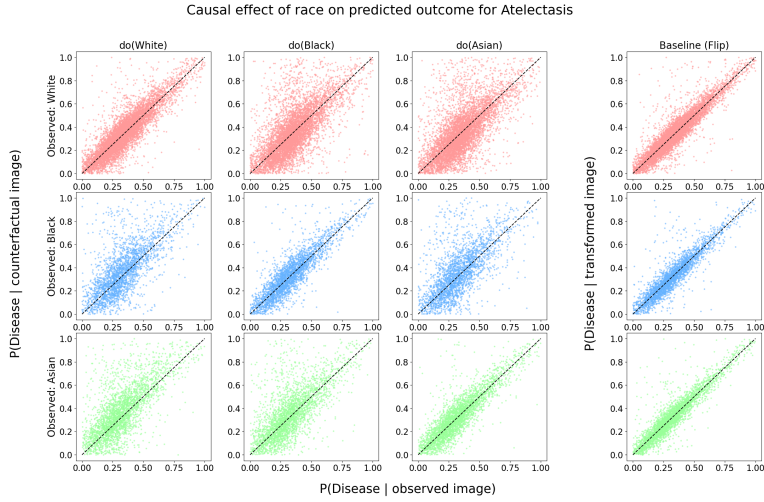


Figure 12: **Impact of the Protected Attribute on Atelectasis Prediction using Counterfactual Images.** Results suggest that when the intervened race is different with the observed race, the predicted outcome has a bias, indicating causal effect of race on the predicted outcome learned by the predictor.

	Cardiomegaly	Edema	Consolidation	Atelectasis	Pleural Effusion
Densenet 121	-2.00	-3.20	0.51	1.49	3.00
	0.0484	0.0018	0.6114	0.1399	0.0032
Densenet 169	3.50	-2.89	-0.45	2.15	4.22
	0.0007	0.0047	0.6564	0.0341	0.0000
Densenet 201	-1.70	-3.90	-0.78	1.04	3.05
	0.0921	0.0002	0.4376	0.3004	0.0029
VGG13	2.56	-2.20	1.23	-1.98	2.80
	0.0122	0.0300	0.2224	0.0510	0.0060
VGG13+BN	-1.05	-1.11	-0.95	-2.89	3.10
	0.2962	0.2695	0.3447	0.0047	0.0024
VGG16	1.03	-3.17	0.56	-2.32	1.40
	0.3051	0.0021	0.5782	0.0223	0.1637
VGG16+BN	-3.11	1.42	2.09	1.40	-2.65
	0.0023	0.1585	0.0390	0.1645	0.0095
VGG19	-2.78	-3.10	1.01	1.76	3.12
	0.0068	0.0024	0.3152	0.0817	0.0023
VGG19+BN	3.00	-2.72	0.66	2.00	2.44
	0.0032	0.0075	0.5111	0.0487	0.0167
Inception V3	-2.35	3.30	-1.19	-2.53	3.05
	0.0210	0.0012	0.2362	0.0131	0.0029

Table 12: Results of the paired t-test for 10 models across 5 diseases on CHEXPert. Each entry shows the t-statistic (top) and p-value (bottom). Significant p-values (< 0.05) are highlighted in red.

J More results on CTF image generation

In Fig. 13-14 we show samples of generated images using a CLDM as in Alg. 1 for both CHEXPert and MIMIC-CXR.

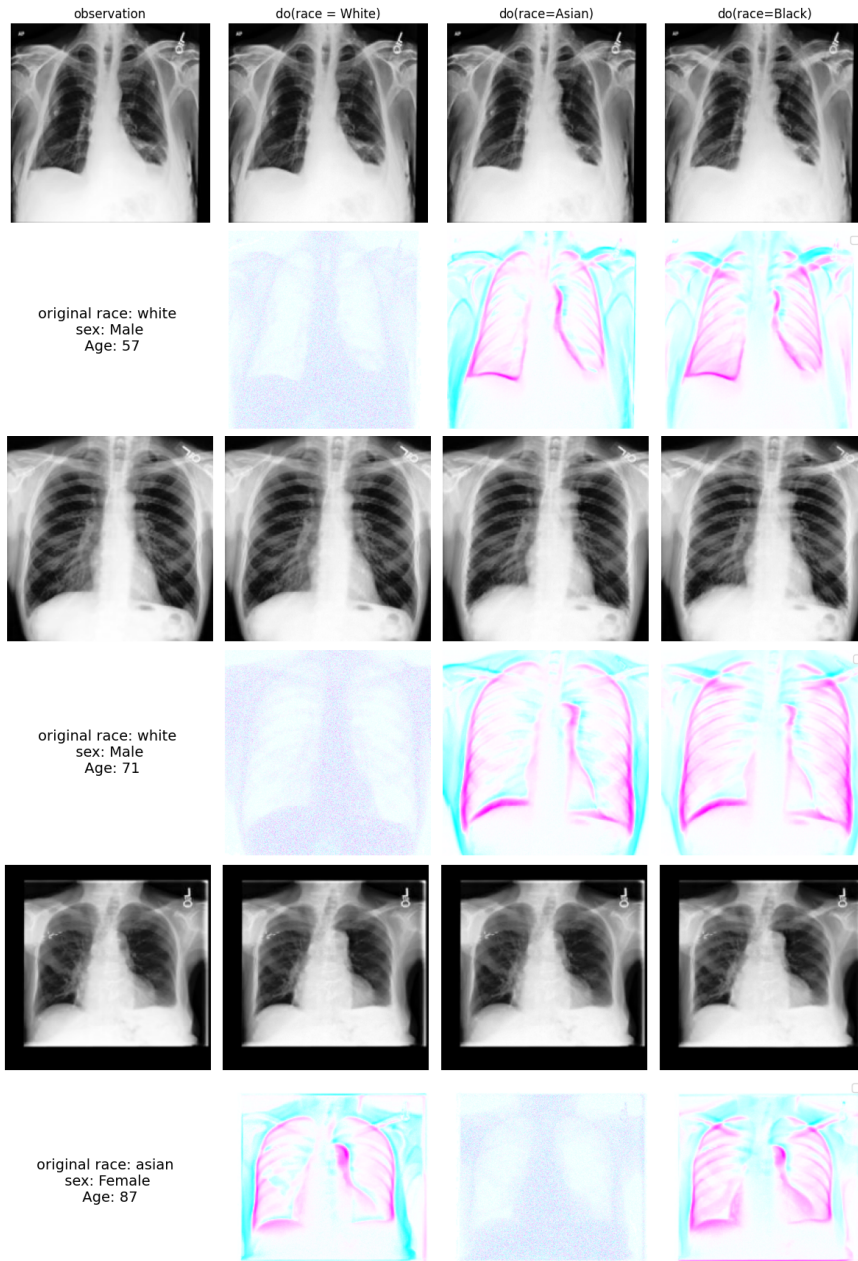


Figure 13: Generated images using a DLDM as in Alg. 1 on CHEXPART. The bottom row highlights differences between the original image and the generated images.

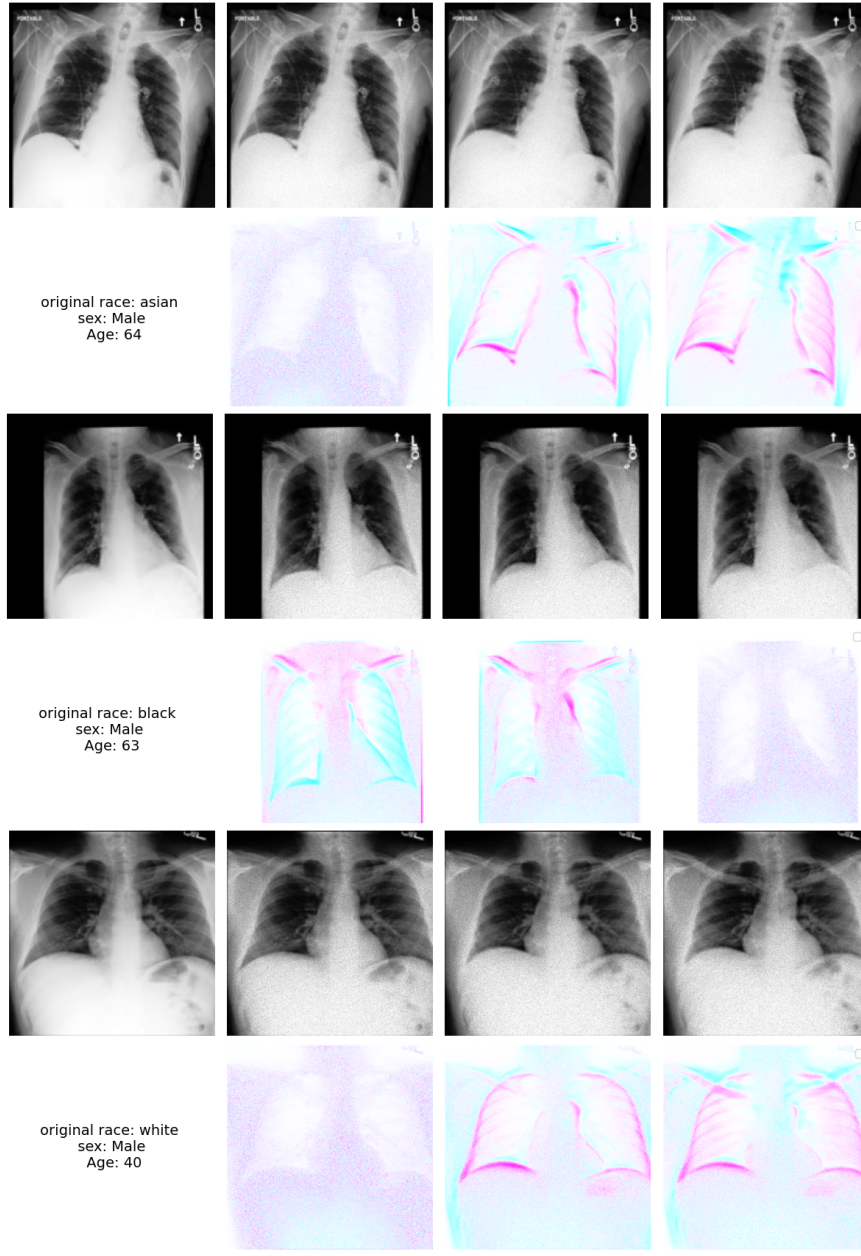


Figure 14: Generated images using a DLDM as in Alg. 1 on MIMIC-CXR. The bottom row highlights differences between the original image and the generated images.

Table 13: Results of the paired t-test for 10 models across 5 diseases on MIMIC-CXR. Each entry shows the t-statistic (top) and p-value (bottom). Significant p-values (< 0.05) are highlighted in red.

	Cardiomegaly	Edema	Consolidation	Atelectasis	Pleural Effusion
Densenet121	1.30 0.1962	-2.70 0.0080	-0.70 0.4840	3.74 0.0003	3.92 0.000093
Densenet169	-2.53 0.0130	-2.57 0.0120	-1.94 0.0556	-2.51 0.01399	3.30 0.0012
Densenet201	2.35 0.0210	0.74 0.4585	-2.39 0.0192	-2.69 0.0082	-3.41 0.00089
VGG13	3.03 0.0030	-2.01 0.0470	-0.90 0.3711	3.44 0.00082	-2.12 0.0367
VGG13+BN	1.89 0.0621	-2.15 0.0340	-0.79 0.4314	2.45 0.01645	3.93 0.000052
VGG16	-2.17 0.0320	1.87 0.0640	0.81 0.4176	3.90 0.00017	2.72 0.0075
VGG16+BN	0.83 0.4051	1.04 0.3000	1.01 0.3152	3.10 0.00241	3.37 0.0010
VGG19	-2.06 0.0422	-1.11 0.2695	-0.92 0.3582	-2.95 0.00387	-3.78 0.00029
VGG19+BN	-1.85 0.0680	-1.80 0.0750	-2.17 0.0320	-2.86 0.0051	3.84 0.00024
Inception V3	2.00 0.0484	2.41 0.0180	0.89 0.3747	2.20 0.0300	2.25 0.0264